aerospace

MDPI

Article

Design and In-Flight Performance of the Power Converter Module and the Pressurised Enclosure for a Scientific Payload Onboard a Stratospheric Balloon

José Luis Gasent-Blesa [1,2], Esteban Sanchis-Kilders [1,2,*], Agustín Ferreres [1,2], David Gilabert [1,2], Julián Blanco Rodríguez [1,2] and Juan B. Ejea [1]

[1] Departamento de Ingeniería Electrónica, ETSE-UV (Escola Tècnica Superior d'Enginyeria—Universitat de València), Avd. de la Universitat sn, E-46100 Burjassot, Spain; jose.l.gasent@uv.es (J.L.G.-B.); agustin.ferreres@uv.es (A.F.); david.gilabert@uv.es (D.G.); julian.blanco@uv.es (J.B.R.); juan.b.ejea@uv.es (J.B.E.)

[2] Spanish Space Solar Physics Consortium, Spain

* Correspondence: esteban.sanchis@uv.es; Tel.: +34-96-354-4029

Abstract

This paper addresses the technical requirements and challenges encountered in the design and development of a customised power electronics board for a stratospheric balloon payload. This board includes power conversion and distribution to critical components (e.g., FPGAs and a ±4 kV power supply), as well as the pressurised enclosure designed to house these components along with other essential electronics. These systems were part of two scientific instruments onboard SUNRISE III, a high-altitude solar observatory launched in July 2024 from ESRANGE (Kiruna, Sweden), with a floating trajectory over the Arctic Circle. The SUNRISE III mission, based on a stratospheric balloon, was carried out by an international consortium of research institutions from Germany, Spain, Japan, and the United States, and in collaboration with NASA's CSBF and the Swedish Space Corporation. Furthermore, this work presents telemetry data from the pressure sensing system of the electronic unit, as well as voltage and current measurements from the power electronics board outputs. These data were recorded during the floating phase of the mission, up to the balloon's arrival in northern Canada after a successful week of scientific operations.

Keywords: stratospheric balloon; power converter; custom design; pressurised unit; scientific payload; solar physics

check for updates

Academic Editor: Hyun-Ung Oh

Received: 29 July 2025
Revised: 6 September 2025
Accepted: 8 September 2025
Published: 12 September 2025

Citation: Gasent-Blesa, J.L.; Sanchis-Kilders, E.; Ferreres, A.; Gilabert, D.; Blanco Rodríguez, J.; Ejea, J.B. Design and In-Flight Performance of the Power Converter Module and the Pressurised Enclosure for a Scientific Payload Onboard a Stratospheric Balloon. *Aerospace* **2025**, *12*, 822. https://doi.org/10.3390/aerospace12090822

Copyright: © 2025 by the authors. Licensee MDPI, Basel, Switzerland. This article is an open access article distributed under the terms and conditions of the Creative Commons Attribution (CC BY) license (https://creativecommons.org/licenses/by/4.0/).

1. Introduction

Balloon-borne platforms offer a cost-effective, recoverable, and operationally efficient means for advancing scientific research and maturing space technologies in relevant near-space environments. Their abbreviated development cycles, reduced regulatory burden, operational simplicity—requiring no propulsion or fuel—make them particularly suitable for early-stage testing of subsystems and payloads intended for orbital deployment. Free-floating balloons equipped with gondolas can reach stratospheric altitudes, enabling exposure to thermal gradients, radiation levels, and low-pressure conditions analogous to those encountered in low Earth orbit. In parallel, tethered configurations remain useful for atmospheric profiling, ground system validation, and communication experiments [1].

While these missions provide notable advantages, they are also subject to technical and programmatic constraints. These include limited environmental qualification, reliance

on non-space-certified commercial components, and tight scheduling driven by funding limitations. Nevertheless, their capacity to generate flight-representative data and accelerate the readiness of novel spacecraft technologies frequently outweighs these drawbacks, supporting their role in bridging the gap between prototypes and space-qualified systems.

Scientific balloons could also be an alternative for planetary exploration, for example for Mars or Venus, as some works have already analysed [2–5]. In the atmosphere, balloon-borne instruments are able to obtain in-situ measurements of wind patterns, greenhouse gases, aerosols, and radiation [6,7], for example. Furthermore, balloons offer astronomers the capability to conduct astronomical observations using telescopes [8], positioned above the dense layers of the atmosphere. Hence, balloons serve as a valuable complement to both satellite-based observations and ground-level measurements. In fact, some of the most important space agencies develop extensive balloon programmes, as the Centre National d'Études Spatiales [9], the Deutsches Zentrum für Luft- und Raumfahrt and the Swedish National Space Agency (BEXUS Programme, in collaboration with the European Space Agency (ESA) [10]), or NASA (Columbia Scientific Balloon Facility, CSBF [11]). The design of the balloon and its altitude take into account the suspended mass of the mission. The NASA standard applied to it is depicted in Figure 1:

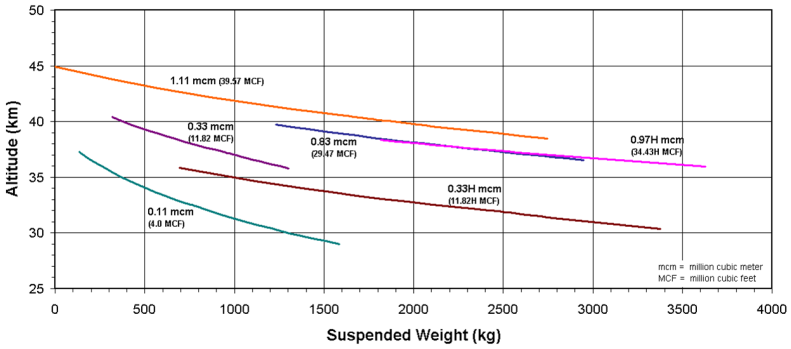


Figure 1. NASA standard design balloon load/altitude curves. Credit: NASA-CSBF.

Works such as [12] describe the different types of scientific balloon opportunities.

Stratospheric balloons typically operate at altitudes ranging from approximately 20 to 50 km, substantially below the Fédération Aéronautique Internationale's Kármán line at 100 km, which conventionally delineates the boundary between atmospheric flight and spaceflight. Made from ultra-thin, helium-inflated polymer envelopes, these platforms support long-duration missions under stratospheric conditions. They enable rigorous endurance testing and functional validation of scientific payloads and technology within an accessible near-space environment. Offering operational flexibility and in-flight payload modification capabilities, stratospheric balloons provide a versatile intermediary stage for research in subjects such as atmosphere and Earth observation, and the maturation of spaceflight technologies [13,14].

Power electronics, including conversion and distribution, is a fundamental system within any scientific payload. Some of the key topics to be considered in its design are efficiency and reliability. The Power Converter Module (PCM) described hereafter had to comply with other important aspects, such as feeding several output lines, belonging to a wide variety of loads, such as Field-Programmable Gate Arrays (FPGA) or a High Voltage Power Supply (HVPS) of ±4 kV, which fed a Fabry-Pérot etalon that tuned the different wavelength samples during the spectral line scan performed by the scientific instrument [15]. The output voltage lines were provided through on-off switches, and several protections were considered in the design due to the criticality of the balloon-borne mission. Furthermore, the Printed Circuit Board (PCB) design had to meet the requirements

of two instruments within a unique layout, in order to save cost and time within a very tight schedule till the mission launch.

The novelty of the proposed PCM would be an architecture mixing discrete design of DC/DC converters and the use of COTS, using the advantages of both approaches, like more flexibility when using a discrete design and more compactness when using COTS. Also, for the discrete DC/DC converter, a new magnetic design technique was used to achieve high inductances with lower turns number by coupling output inductors together.

This strategy aligned with the decision to rely primarily on commercial electronic components, providing enhanced design flexibility, shortened procurement lead times and cost reduction is well suited to a stratospheric balloon mission. Notwithstanding these advantages, several critical factors must be mitigated to ensure reliable performance at altitude. Of particular importance is the requirement that the electronic unit (E-Unit) be housed within a sealed, pressurised enclosure filled with dry air or nitrogen, in order to prevent condensation and humidity-related malfunctions under low-pressure and variable-temperature conditions [16]. Another critical point is the operating temperature and the thermal issues that defined the E-Unit coating. Even more critical is the ascent temperature profile, which drops below $-50\,^{\circ}$C. In addition, a mission with optical elements leads to strong constraints in the bill of materials, focusing the problem on outgassing parameters. The O-ring material selection that seals the two halves of the enclosure of the Electronic unit was a critical step [17]. Moreover, to allocate a High Voltage (HV) connector for ± 4 kV, facing a close-to-vacuum environment outside (close to the minimum of Paschen's law, i.e., significant risk of arcing), was also a critical issue in the project. That is why a tailored design had to be produced.

The paper is organised as follows. Section 2 provides an overview of the SUNRISE III mission, summarising its objectives, payload configuration, and launch site characteristics. System-level requirements guiding the design process, with a particular focus on the electrical and mechanical constraints during the critical ascent phase, are outlined in Section 3. Section 4 discusses the development of the Tunable Magnetograph (TuMag) PCM, detailing its topology, key magnetic components, and manufacturing. It is important to note that this design was intended to be flexible, requiring limited modifications to satisfy the requirements of another mission instrument (SUNRISE Chromospheric Infrared spectro-Polarimeter, SCIP), thereby optimising cost and development time. The pressurised enclosure of the E-Unit is examined in Section 5, addressing sealing strategies, interfaces with the high-voltage board, material selection, surface treatments, and integration. Structural performance under representative loading conditions is assessed in Section 6 through Finite Element Analysis (FEA). Finally, Section 7 presents in-flight telemetry data confirming nominal system operation and validating the reliability and stability of the design throughout the mission.

2. SUNRISE III Mission

2.1. Background and Launch Site

One of the most notable examples of a balloon-borne observatory is the SUNRISE project, a dedicated solar research platform designed to investigate the Sun's magnetic field and the convective plasma flows in its photosphere and chromosphere. Understanding these fundamental processes is essential for deciphering the Sun's magnetic activity and its influence on space weather, including solar eruptions and coronal mass ejections, which can have significant effects on Earth's environment. The SUNRISE project involves three missions: SUNRISE I, SUNRISE II, and SUNRISE III [18–20].

By operating at altitudes of around 37 km in the stratosphere (altitude profile of SUNRISE III depicts in Figure 2), above more than 99% of the Earth's atmosphere, SUNRISE

avoids the image distortion caused by atmospheric turbulence and gains access to ultraviolet wavelengths as low as 200 nm. This allows for clearer and more detailed observations of the Sun. The mission's unique position also offers continuous solar observations for several days, thanks to the launch trajectory along the Arctic polar region during solstice conditions. By combining the benefits of both, space-based telescopes—offering undisturbed views from above the atmosphere—and ground-based instruments, the SUNRISE mission delivers high-quality data at a fraction of the cost of space missions. Furthermore, the instrument can be recovered, refurbished, upgraded, and relaunched as in SUNRISE I and SUNRISE II, adding to the mission's cost-effectiveness. Therefore, SUNRISE provided almost seeing-free observations, with stable observing conditions and long time data series from the multi-wavelength payload data without atmospheric refraction, and including near-ultraviolet observations.

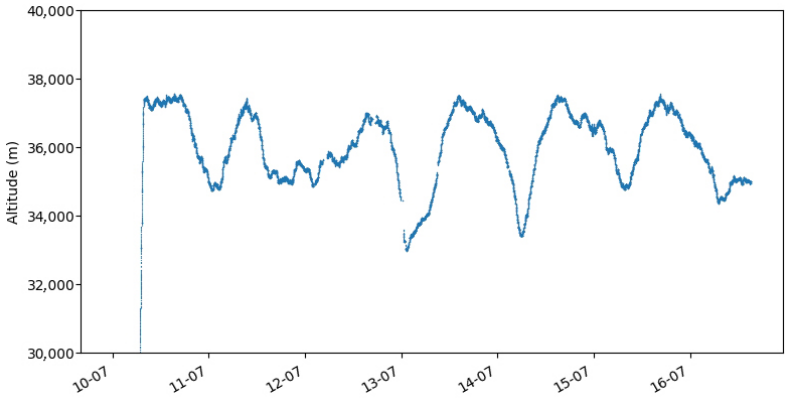


Figure 2. SUNRISE III altitude, 2024. Credit: SUNRISE III.

The SUNRISE observatory comprised a one-metre aperture solar telescope—the largest of its kind ever launched from Earth—along with a suite of science instruments. It was also equipped with a beam stabilisation system, and a Correlating Wavefront Sensor (CWS) providing active image correction. These components were supported by a gondola platform integrating the main onboard computer and data storage systems [18–21]. The telescope incorporated in-flight alignment and image stabilisation mechanisms, delivering near diffraction-limited performance and achieving spatial resolutions below 100 km on the solar surface. This high level of precision enabled unprecedented observations of solar magnetic structures and dynamic processes.

SUNRISE successfully completed two flights, one in 2009, which faced minimum solar activity, and another in 2013, with higher solar activity. Together, these missions contributed significantly to advancing our understanding of the Sun's lower atmosphere. These two missions were developed by an international consortium led by the Max-Planck-Institut für Sonnensystemforschung (MPS, Germany), with collaboration from research centres of Spain, Germany, and the USA. It is noteworthy that one of the instruments onboard SUNRISE I and SUNRISE II, the Imaging Magnetograph eXperiment (IMaX), completely developed by a Spanish Consortium, was the forerunner of the Polarimetric and Helioseismic Imager (PHI), onboard the Solar Orbiter satellite [22,23].

The SUNRISE missions are part of NASA's Long Duration Balloon (LDB) program, part of the CSBF activities. Its helium balloon had a volume of approximately one million cubic meters. At the beginning of the project, SUNRISE I was foreseen to be launched in the Antarctic, from McMurdo facilities (USA) [24], but finally they were launched from the ESRANGE Space Center facilities of the Swedish Space Corporation near Kiruna (Sweden).

Based on data compiled by the StratoCat website [25], a well-established repository that provides detailed information on stratospheric balloon activities, the total number of

stratospheric balloon launches is estimated to be more than 15,000 since around the middle of the 20th century. One of the most important sites for this kind of launching is ESRANGE (Kiruna, Sweden) [26], from the Swedish Space Corporation (SSC). This facility has been in operation since 1966, and it includes, among others, capabilities for satellite launches and rocket engine testing, and high altitude balloons, being the first site in mainland European Union with orbital launch capability. Furthermore, it also locates satellite ground stations. Since 1974, more than 600 stratospheric balloons have been launched from this site, including payloads of several tons. Between mid-May and mid-July, the stratospheric winds remain stable from the east, making this an optimal time for medium- to long-duration balloon flights, including those crossing the Atlantic. In addition, being located above the Arctic Circle (about 200 km), the midnight Sun is available during those dates. This means that the Sun is continuously visible 24 h a day, thus providing perfect conditions for solar physics missions.

Figure 3 shows the ESRANGE site (left) and the SUNRISE I launch (right).

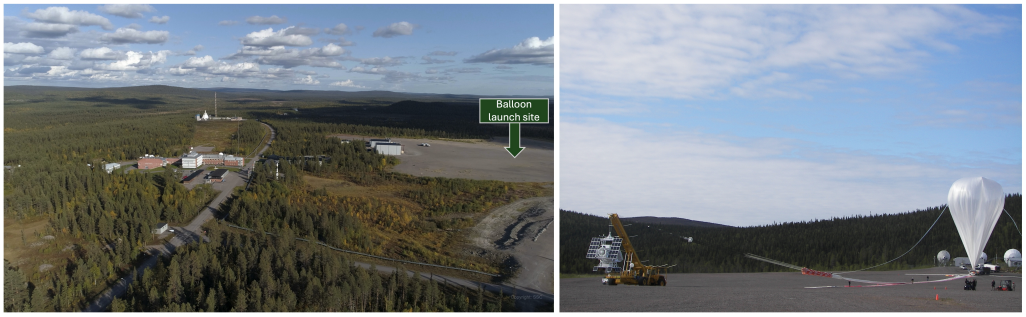


Figure 3. (**left**) ESRANGE Space Center view. Credit: SSC. (**right**) SUNRISE I launching. Credit: J.L. Gasent.

2.2. SUNRISE III Payload

The SUNRISE III balloon-borne solar observatory represents a significant advancement within a long-standing international collaboration, led by the MPS in partnership with the Johns Hopkins Applied Physics Laboratory (APL, USA).

Building upon the legacy of SUNRISE I and II, the current mission was conceived to perform high-resolution solar observations from the stratosphere. It features a fully reengineered gondola that integrates a one-metre telescope, a new scientific payload of three state-of-the-art instruments, and a high-precision image stabilisation system. These enable a significant improvement in image quality and measurement capability.

Principal scientific and institutional partners include a Spanish consortium, the National Astronomical Observatory of Japan (NAOJ), and the Leibniz-Institut für Sonnenphysik (KIS, Germany), with operational and logistical support provided by NASA's Wallops Flight Facility Balloon Program Office (WFF-BPO) and the SSC. Notably, SUNRISE III marks the first participation of Japan in the mission, thereby expanding the international scope of the collaboration compared to SUNRISE I and SUNRISE II. The SUNRISE III gondola was developed by the Johns Hopkins University Applied Physics Laboratory (APL) [21].

The Spanish Consortium is entitled 'Spanish Space Solar Physics Consortium' (S^3PC), and is formed by the Spanish research institutes Instituto de Astrofísica de Andalucía (IAA-CSIC), Instituto Nacional de Técnica Aeroespacial (INTA), Universitat de València (UV), Universidad Politécnica de Madrid (UPM), and Instituto de Astrofísica de Canarias (IAC) under the leadership of IAA [27]. This Consortium is responsible for the whole TuMag instrument and for the E-Unit of the SCIP instrument, which is led by the NAOJ, and includes contributions from Japan Aerospace Exploration Agency (JAXA) and MPS.

The mission's maiden launch attempt was conducted in July 2022. Nevertheless, due to an anomaly detected during the ascent phase, the mission was aborted after only a few hours of flight. Upon recovery at the landing site near the Norwegian border, thorough inspections verified that no significant damage had been sustained by either the telescope or the scientific instrumentation. Despite this, a detailed evaluation of the scientific payload was performed, which concluded that only minor refurbishment was required in order to prepare for a forthcoming flight [20].

Finally, SUNRISE III was launched on 10 July 2024, and after a flight of almost a week above the Arctic Circle it landed in Canada.

The landing sites of the preceding missions were likewise located in northwestern Canada.

SUNRISE III enhanced significantly the two previous missions, mainly in terms of image stability, duration, gondola features, and payload capabilities [20]. Moreover, the instruments onboard were developed by means of new and improved designs in almost all the systems compared to the previous SUNRISE missions.

Additionally to the telescope, the Image Stabilization and Light Distribution System (ISLiD) and the CWS, SUNRISE III allocated the following scientific payload:

- SUSI is an ultraviolet, slit spectropolarimeter covering the near-ultraviolet range between 300 nm and 410 nm, which is to a large extent poorly accessible from the ground. It studied the coupling between the various layers of the solar atmosphere. MPS developed this instrument with contributions from NAOJ [28].
- SCIP is an infrared slit spectropolarimeter able to observe in two spectral regions around 768.5 nm and 851.5 nm. It measured the chromosphere, and combines the information with lines formed in the deep to upper photosphere. The instrument was under NAOJ and S^3PC responsibility [29].
- TuMag is a new magnetograph and tachograph, able to image the polarisation properties of three spectral lines in the visible: Fe I @ 525.02 and 525.06 nm; and Mg Ib2 @ 517.3 nm. It delivered 2D maps of two different layers in the solar atmosphere, the deep photosphere and the chromosphere, at high temporal cadence. The instrument was developed by S^3PC [15].

The TuMag instrument concept was also an important background for the Coronal Magnetograph (CMAG) mission proposal [30].

Figure 4 displays the location of the telescope, the scientific instruments and their electronic units at the E-racks (left), as well as the mission trajectory provided by the CSBF website (right).

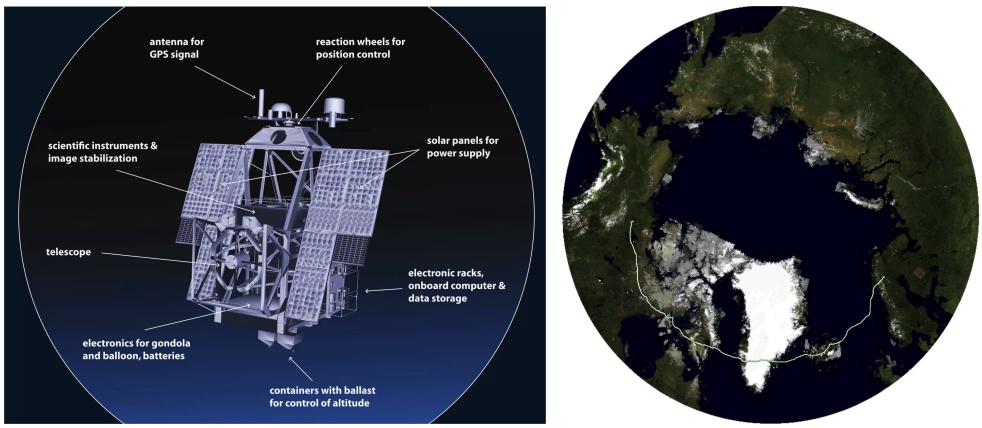


Figure 4. (**left**) SUNRISE III front view. Credit: MPS. (**right**) SUNRISE III trajectory, from ESRANGE to north Canada. Credit: CSBF.

3. Requirements Review

3.1. Mission Requirements

The environmental specifications for the E-Unit were mainly driven by the thermal conditions encountered during ascent, as well as the ambient pressure sustained throughout the flight. The ascent phase of a stratospheric balloon typically spans, depending on the float altitude, between one and four hours, a relatively short period in contrast to the overall mission duration. The study of the ascent phase is a key point from the thermal point of view, where several parameters have to be considered [31]. During this phase, the payloads are subjected to extremely harsh conditions, primarily resulting from the convective cooling that occurs as the balloon moves through the cold atmosphere, where minimum temperatures are encountered in the tropopause (around 10–20 km). In fact, the predicted atmospheric air temperature drops below $-50\,^{\circ}\mathrm{C}$ (even down to $-70\,^{\circ}\mathrm{C}$). The temperature profile during the ascent phase is extremely dependent on the launch site, the epoch, the height of the floating phase, and the launch time [32–35]. In fact, in general, the height range of the troposphere depends to a large extent on the geographical situation, the season and the meteorological situation [36].

The floating height of the mission implies an atmospheric pressure of around 0.003 bar. At that pressure, the outgassing features of the materials are critical due to the payload onboard the gondola including several optical elements.

Considering that the budget for this type of mission is only a small fraction of that for spaceborne missions, the design of the electronic systems is based on commercial componets, also known as Commercial Off-The-Shelf (COTS) components. Consequently, the electronic boards have to be housed in a pressurised enclosure with a tight temperature control. This measure ensures the proper operation of commercial devices without concerns related to near-vacuum conditions determined by the floating height of the balloon. Moreover, the development timeline was critical in this project: the use of not space-qualified components and tools reduces the engineering efforts required compared to a large space mission.

As a summary, all these requirements had an impact on the design of the instruments, in the selection of electronic components and materials, and also in the thermoelastic loads and the overpressure effects during the floating phase.

3.2. E-Unit Power Electronics Requirements

The PCM had to integrate both the power conversion and distribution stages, playing a critical role in managing power requirements across multiple subsystems.

The input voltage requirement for the PCM is based on the gondola's nominal unregulated range of 20.4 V to 29.2 V. Additionally, the PCM is linked to a Latching Current Limiter (LCL), which limits the peak current up to 25 A, providing also fundamental protection to the instrument. The PCM had to interface with other E-Unit subsystems through an internal housing harness, while connections to the Optical Unit (O-Unit) and the SUNRISE III gondola platform are made via feedthrough connectors, ensuring seamless power distribution.

To mitigate electromagnetic interference, the PCM had to incorporate an Electromagnetic Interference (EMI) filter, including a Common Mode (CM) and Differential Mode (DM) filters, ensuring compliance with stringent standards. Furthermore, the PCM always started under identical conditions, even after a restart. The PCM was required to ensure galvanic isolation between its primary and secondary sides.

The PCM feeds after its EMI filter the Data Processing Unit (DPU), Analog, Mechanisms & Heaters Drivers (AMHD), HVPS, Mechanisms (regulated 24 V), Heaters, and Cameras, while in the SCIP E-Unit, it powers the DPU, AMHD, Cameras, Heaters, Scan

Mirror Mechanism (SMM), and Polarization Modulation Unit (PMU). It should be noted that the Heaters (in both TuMag and SCIP), as well as the SMM and the PMU are powered from the PCM primary side, i.e., directly from the bus voltage.

The required voltages and powers are collected in Table 1. Without considering the contribution of the PCM to the power budget, the required total power of TuMag was 167 W and that of SCIP was 128 W.

Table 1. PCM voltages and power required by each instrument.

Voltage	TuMag-Power	TuMag-Subsystems	SCIP-Power	SCIP-Subsystems
+3.3 V	5.15 W	DPU, AMHD	5.15 W	DPU, AMHD
+5 V	4.65 W	DPU, AMHD, HVPS	3.75 W	DPU, AMHD
+12 V	45.0 W	DPU, AMHD, HVPS	36.75 W	DPU, AMHD
−12 V	0.75 W	AMHD	0.50 W	AMHD
+24 V	4.50 W + 32.0 W	Cameras & Mechs, HVPS	6.75 W	Cameras
Bus voltage (V_{in})	7.05 W	Heaters	46.0 W	Heaters
Bus voltage (V_{in})	–	–	22.0 W + 7.0 W	SMM, PMU

The minimum efficiency of the PCM required in the corresponding operational mode for either TuMag or SCIP was 80%.

The power distribution circuit had to allow individual switching of subsystems, except for the DPU and AMHD, offering flexibility in power management. Voltage regulation remains within a 5% tolerance, and ripple is maintained below 1%, ensuring stable operation. The PCM also had to include voltage and current sensing for both the input and secondary outputs, as well as temperature sensors located near critical components—four for TuMag and three for SCIP.

Key protection features include Under-Voltage Lock-Out (UVLO) and Over-Voltage Lock-Out (OVLO) with thresholds that encompass a broader input range, along with overcurrent (OC) protection on both the primary and secondary output lines to avoid any catastrophic problem. The core of the PCM is based on a custom-designed converter, integrated into a double-sided PCB. Although the components are primarily commercial, they are selected for extended temperature range operation, ensuring reliability in the harsh conditions of a stratospheric balloon-borne mission.

The thermal interface point between the E-Unit and the platform was defined within a range of −35 °C to 35 °C, including contingency. Based on this definition, and following the corresponding thermal analysis, both the lower and upper component temperature limits achieved a margin of 10 °C with respect to their temperature limits.

The PCM's envelope measures 250 × 250 × 40 mm, including the populated double-sided PCB. The allocated mass of that PCB was 1.0 kg, with a target of 0.85 kg. The PCM had to be mechanically attached using M3 screws. Both, the TuMag and SCIP PCMs share a common layout, maintaining compatibility within the designated envelope. While several components' references are shared between both PCMs, some differ to suit the specific needs of each subsystem and load requirements.

3.3. E-Unit Mechanical and Structural Requirements

The main electronics for the TuMag and SCIP instruments had to allocate their electronic boards, the feedthrough hermetic connectors and the internal PCB interconnection harness, keeping a common design between both instruments in order to reduce the cost and the development period.

As previously described, the E-Unit electronic boards were housed within a pressurised enclosure to mitigate issues arising from the use of standard electronics not rated for low-pressure environments. In addition, humidity within the unit had to be strictly

avoided. Consequently, a purging and venting system was required to fill the enclosure with nitrogen.

Moreover, the E-Unit had to be equipped with the appropriate connectors to support both data transmission and power supply functions, including low- and high-voltage interfaces. With the exception of two connectors designated for the AMHD module and one dedicated to grounding, all connectors had to be positioned on a single side wall. Most of the interfaces had to utilise sub-D connectors, while the high-voltage connections (±4 kV) had to be implemented using two coaxial connectors. A specifically dedicated gasket was required to ensure the proper mounting and sealing of these coaxial interfaces.

The mass requirement for the E-Unit Housing amounted to 18.3 kg, which includes a 10% contingency margin. This total also accounts for the mass contributions of the feedthrough connectors, O-rings, fastening elements, and valves. As for the envelope, the maximum dimensions were specified as 585 × 405 × 230 mm.

Concerning the outgassing limits, a key demand of any of the SUNRISE III systems because of the optic elements, the limits were fixed at 1% for the Total Mass Loss (TML) and Recovered Mass Loss (RML), and 0.1% for the Collected Volatile Condensable Material (CVCM).

The thermal behaviour of the E-Unit is out of the scope of this work, but some thermal considerations had an impact on the mechanical design and materials and coating selection, as well as on the thermo-elastic loads during the ascent phase. The emissivity, at least of 0.8, together with the mentioned outgassing levels, was the driver for the painting selection. In addition, a thermal filler was required to be placed between the E-Unit and the platform to maximise the thermal conductivity. Additionally, the electrical conductivity among all the elements of the E-Unit had to be guaranteed and maximised to avoid any metallic isolated part.

The main requirements to be fulfilled related to the structural analysis were as follows:

- The deformation of any PCB due to any kind of load had to be lower than 0.4 mm, which is based on the heritage from previous payload development, such as [18,19,22].
- The O-rings had to be compressed at least 10% (i.e., 0.5 mm for the main flange).

There were no further requirements in terms of stress values in the PCBs.

Table 2 collects the load cases and the associated Factor of Safety (FoS) demanded in this project:

Table 2. Load cases considered in the E-Unit structural analysis.

Load Event/Nature	Level	Yield Limit FoS
Quasi-static load X-axis	8 g	1.25
Quasi-static load Y-axis	6 g	1.25
Quasi-static load Z-axis	5 g	1.25
Pressure loads	1.27 bar [1]	1.50
Thermo-elastic, Hot case	65 °C [2]	1.25
Thermo-elastic, Cold case	−70 °C [2]	1.25

[1] Worst case temperature, 65 °C, produces an overpressure of approximately 0.17 bar over the nominal value, 1.1 bar. [2] Thermo-elastic loads were obtained considering a reference temperature of 20 °C.

Finally, although no stringent cleanliness requirements were imposed on the E-Unit, it was essential to ensure that its external components and materials did not introduce particulate contamination to the optical elements, and that all materials were carefully selected to minimise outgassing.

4. TuMag PCM

4.1. Design Overview

The PCM provides the necessary output voltages for the TuMag instrument, primarily through a custom DC/DC converter implemented on a double-sided PCB populated with commercial-grade components rated for extended temperature ranges.

Taking into account the requirement concerning the input voltage limits detailed in Section 3.2, the PCM input bus supports a wider range from 19.0 V to 30.0 V.

A power distribution stage delivers generated voltages to TuMag subsystems, allowing individual on/off control via switches managed by the DPU. Protection features include UVLO, OVLO, a Primary OC detector, and secondary-side OC protections. A simplified block diagram of the TuMag PCM is displayed in Figure 5.

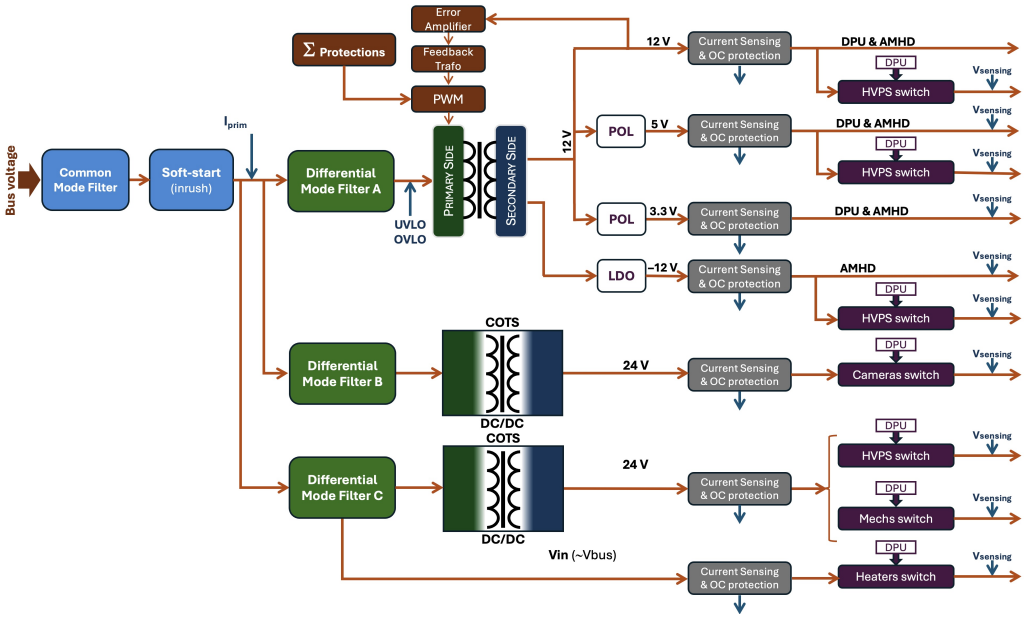


Figure 5. Simplified PCM block diagram.

The PCM contains three DC/DC converters: DC/DC A (main converter), DC/DC B, and DC/DC C:

- DC/DC A is a custom converter, powering the DPU, AMHD, and HVPS.
- DC/DC B supplies an isolated +24 V line to the cameras using a COTS switching converter.
- DC/DC C powers heaters and provides +24 V output for HVPS and Mechanisms via a COTS switching converter.

The DC/DC A operates at a fixed switching frequency of 125 kHz via an RC oscillator, while the COTS units operate at 320 kHz.

The primary side of the main converter (DC/DC A) includes a soft-start, a two-stage EMI filter, UVLO/OVLO protection, and a Primary OC protection, all interfacing with the Pulse Width Modulator (PWM) controller. The main converter employs a forward topology with galvanic isolation, featuring dual control loops: peak current control and voltage regulation referenced to +12 V. The transformer generates +12 V and −12 V outputs, from which other voltages (except 24 V) derive.

The feedback philosophy is designed to regulate the +12 V output of DC/DC A, which serves as the reference for the main voltage control loop. An error amplifier located on the secondary side compares the actual output with a reference voltage. The resulting error signal is transmitted via a transformer to the primary side, where it modulates the PWM

controller. This transformer operates synchronously with the main switching transistor to preserve timing accuracy. Peak current sensing is also implemented on the primary side, enabling the UC3845BD1 PWM controller to perform real-time current-mode control, thereby enhancing system stability and transient response.

Therefore, among the secondary outputs, only the +12 V line is fully regulated via the main feedback loop. Consequently, the remaining outputs are subject to cross-regulation effects, whereby their voltage levels may vary depending on load changes, even when the +12 V output remains stable. To meet the stringent load and line regulation requirements, post-regulation is applied to specific outputs:

- The −12 V line uses a Low-Dropout (LDO) regulator (LM2991S, Texas Instruments), selected for its low dropout voltage and stable performance across varying conditions.
- For both the +3.3 V and +5 V outputs, Point-of-Load (POL) converters are employed for improved efficiency compared to LDOs. These are powered from the +12 V rail and use the OKX-T/5-D12 module by Murata, configured according to the manufacturer's guidelines.

Both DC/DC B and DC/DC C use isolated +24 V COTS converters powered from the primary side, specifically the TRACO TEP 100-4815WIR module rated at 4.2 A.

Each subsystem power line, with the exception of the DPU and AMHD, is equipped with an ON/OFF switch and its corresponding driver circuitry; a simplified block diagram of the switching concept is shown in Figure 6. These switches enable individual activation or deactivation of the power outputs.

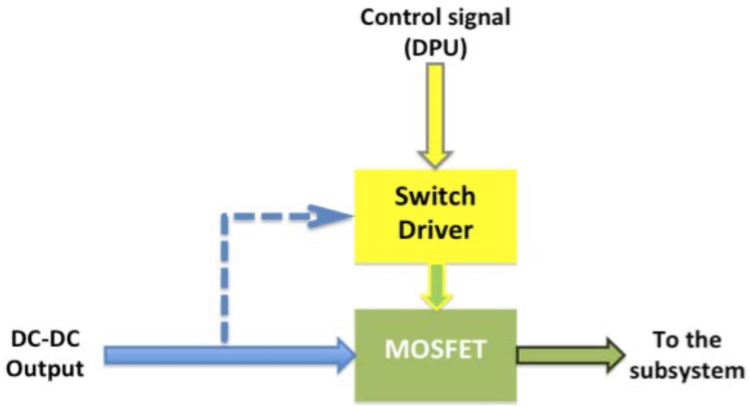


Figure 6. Simplified block diagram of the switching unit.

Control signals for the switches are such that a single command from the DPU governs all power lines within a specific subsystem. This approach simplifies control and reduces layout complexity by limiting each subsystem to a single enable signal. It is important to remark that all the switches were designed in order to control the rise times of the proper output voltages within the specified times, especially to avoid too large inrush currents into the subsystems.

The PCM board interfaces with the gondola's primary voltage supply via a Sub-D 15-pin connector. Additionally, an 80-pin connector links the PCM to the remainder of the E-Unit electronics, excluding the HVPS. To interface electrically with the HVPS, the PCM features a dedicated 12-pin connector, facilitating seamless integration within the power distribution architecture.

4.1.1. Overcurrent Protection, Shut-Down Events, and Auto-Reset

The main DC/DC, converter A, includes a current sensor and an OC detector for each of its output lines (+3.3 V, +5 V, +12 V, or −12 V), which triggers the OC signal (OCa).

DC/DC B provides a regulated 24 V output to the cameras, while DC/DC C supplies 24 V to the heaters, HVPS, and mechanisms. Likewise, switching for each voltage output is independently controlled by the DPU, with integrated OC protection provided via the OCb and OCc signals, respectively. It should be pointed out that an OC in DC/DC A also disables DC/DC B and DC/DC C.

The PCM incorporates several protection Mechanisms capable of initiating a full system shut-down. These include the following:

- Detection of an OC condition on the primary side.
- UVLO/OVLO events on the input bus.
- A trigger on the OCa.

Upon the activation of any of these faults, the PCM halts operation immediately to preserve system integrity. Recovery is managed autonomously through a timed reset sequence, ensuring the system restarts in a stable configuration once fault conditions are cleared.

The PCM does not have a dedicated ON/OFF command interface; instead, it powers up automatically once the input voltage surpasses a predefined threshold. Consequently, following any protection-triggered shutdown, the PCM initiates an autonomous reset sequence.

This reset occurs after a delay of approximately 100 to 200 ms. This interval ensures that the PCM restarts each subsystem under controlled and consistent conditions, preventing repeated fault cycles (hiccup effect) and enabling recovery from transient disturbances.

4.1.2. Input Section and EMI Filters

The input stage of the PCM also serves as the interface to the SUNRISE III gondola power system via the LCL. The circuit begins with a CM EMI filter and a Transient Voltage Suppression (TVS) device for overvoltage protection. To manage inrush current, a MOSFET is used in conjunction with an RC network that provides a controlled turn-on delay when input voltage is detected.

Following this stage, the input current flows through a current sensor and proceeds to DM input filters specific to DC/DC A, B, and C. After the DM filter of DC/DC A, a linear Auxiliary Power Supply initiates the start-up sequence.

The input filter for DC/DC A consists of three cascaded stages: a CM coupled inductor shared by all converters, a pair of CM capacitors, and two series-connected DM filter stages. Additional high-frequency filtering is implemented at the input of DC/DC A to mitigate switching noise. The second DM stage also includes CM capacitors and damping elements.

The input filters for DC/DC B and DC/DC C are similarly structured, featuring two cascaded DM stages following the shared CM filter. Each set feeds its respective converter while providing noise attenuation tailored to its power profile.

4.1.3. Telemetry

Current and voltage sensing signals are multiplexed and transmitted to the AMHD, which controls the multiplexor selection. To enhance noise immunity, signals are converted from voltage to current prior to transmission.

Primary side sensing signals are conveyed across galvanic isolation via a voltage/current converter, ensuring signal integrity. The PCM incorporates four temperature sensors monitoring critical components, with readings directly managed by the AMHD.

Additionally, the PCM provides two status signals to the DPU:

- OCb status: Indicates activation of the OC protection on the DC/DC B line, corresponding to the +24 V camera power exceeding its threshold.

- OCc status: Represents the OC status for DC/DC C outputs, covering heaters, HVPS, and mechanisms. This signal results from an OR function combining all relevant OC detections and includes conditioning circuitry.

The AMHD manages two 16-channel multiplexors within the PCM, enabling selection of required sensing channels via four control signals and one enable signal, facilitating robust and flexible monitoring.

4.1.4. Magnetic Components

The DC/DC A converter, which is custom designed unit provides three 12 V outputs, namely a roughly 50 W output and two additional 12 V outputs of 1.5 W each, to feed control circuits on primary and secondary. Primary and secondary output voltages are galvanically isolated. Due to the low power management, a FORWARD topology was selected for the DC/DC A converter. A FORWARD topology in continuous conduction mode also provides lower switching currents and therefore lower electromagnetic noise, a stable behaviour due to being a BUCK derived topology and a better cross regulation compared to other topologies like multioutput FLYBACK converter.

On the other hand, a FORWARD converter needs output filter inductors in each of its outputs and a novel technique developed by the authors [37–39] achieving close to zero ripple current has been applied.

In this section the magnetic design of the output inductors and how to reach near-zero current ripple is briefly described. It is well-known that coupling output inductors in BUCK type topologies can provide zero current ripple and the authors have concluded [37–39] under which conditions this phenomenon appears. In fact, zero current ripple is only possible in all but one output. Therefore, the high-power output has been selected as the regulated output with non-zero current ripple and the other two outputs are designed to have near-zero current ripple.

Zero current ripple is achieved when the equivalent output inductor tends to infinity, due to the coupling effect. In fact, the normalised equivalent output inductor is described by the following expression:

$$\overline{L_{eq_q}} = \frac{\left[(m-1)\tilde{k}+1\right](1-\tilde{k})}{\left[(m-2)\tilde{k}+1\right] - \tilde{k}\sum\limits_{\substack{r=1 \\ r\neq q}}^{m} \Delta_{qr}} \tag{1}$$

where m stands for the number of windings coupled together, m = 3 in our case, $\tilde{k}$ stands for the approximate overall coupling coefficient of the windings, $\tilde{k}$ = 0,8 in our case and finally Δ_{qr} stands for the deviations from the ideal coupled inductors. Δ_{qr} is ideally 1 but has different values in real designs and circuits due to voltage unbalance applied to the inductors, time differences applied to each winding and other divergences from the ideal case.

Ideally (Δ_{qr} = 1) the equivalent inductance of each output would be

$$\overline{L_{eq_q}} = (m-1)\tilde{k}+1 \tag{2}$$

If the coupling coefficient is one ($\tilde{k} \to 1$),

$$\overline{L_{eq_q}} \overset{\tilde{k}\to 1}{=} m \tag{3}$$

And the equivalent inductance is at the most equal to the number of windings coupled together times its inductance value.

But in real life, the deviations exist, and the expression given before for the equivalent inductance applies. The expression then clearly shows that a pole exists that can make the equivalent inductance infinite and therefore achieve zero current ripple for this output. Figure 7 shows clearly the pole and at which coupling coefficient the equivalent inductances of L_{eq_2} and L_{eq_3} tend to infinity. On the other hand, L_{eq_1} drops and does not reach an infinite value.

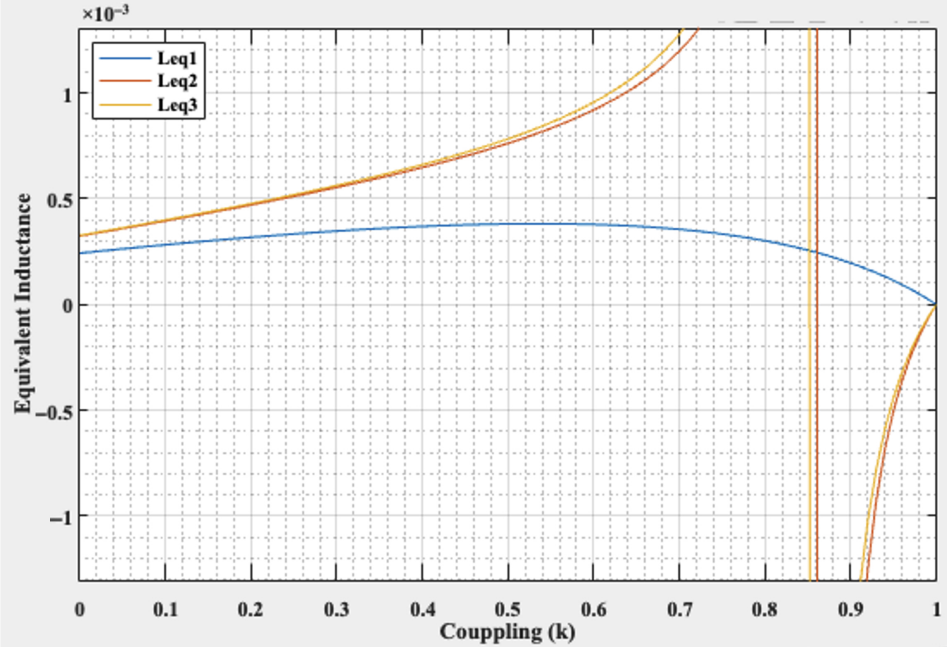


Figure 7. Equivalent inductance L_{eq_q} vs coupling factor k.

The design technique [38] is then to adjust the coupling coefficient to come as close to the pole as possible. In this case, and following the Figure 7, a $\tilde{k}$ = 0.8 is chosen.

Using a low permeability (μ = 90) MPP toroidal core and winding the three inductors on a different sector, results in a "bad" coupling of $\tilde{k}$ = 0.8.

Table 3 shows the required inductance based on the maximum current ripple of each output, the measured inductance of each winding of the coupled inductor and finally the equivalent inductance of each output using Equation (1).

Table 3. Required inductance.

Inductance	Vout	$Lo_{required}$ (μH)	$Lo_{measured}$ (μH)	$Lo_{equivalent}$ (μH)
L1	+12V0	240	242	300
L2	−12V0	1800	323	2110
L3	+12V0 aux	1800	326	2500

Current ripple is not zero but tends to and reduces switching noise and the need for a large output capacitor. Choosing a coupling coefficient $\tilde{k}$ closer to 0.87 would bring the design closer to the infinite inductance point, but it has to be considered that this is a very unstable point (see Figure 7) and small changes of $\tilde{k}$ result in large changes of the equivalent inductance. Therefore, a conservative design was chosen.

This novel technique has been successfully implemented in both the TuMag and SCIP instruments, demonstrating excellent performance during laboratory PCM testing, instrument-level verification, and in-flight operations. It has therefore served as a technological demonstrator of the underlying theoretical developments and is now positioned as a

promising approach for future space missions, where the optimisation of limited resources remains a critical objective.

4.2. Manufacturing and Test

The TuMag PCM was fully integrated and tested at the UV premises, before its integration in the E-Unit. The FM PCM fitted with the defined envelope and its mass was 810 g, below the defined limit. The model philosophy of a balloon-borne project is simplified with respect to a large space mission [40]. In fact, just a Breadboard (BB) and a Flight Model (FM) were developed in SUNRISE III; the FM is shown in Figure 8.

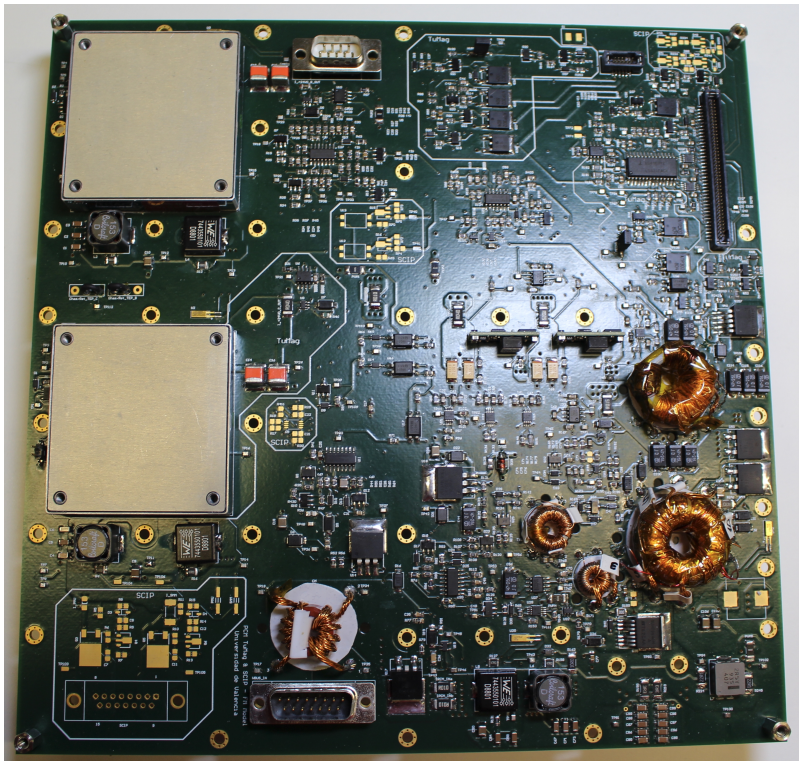


Figure 8. TuMag PCM FM at the UV premises.

The Electronic Ground Support Equipment (EGSE) comprised the test equipment and two auxiliary boards specifically designed for the PCM verification, in order to simulate the loads presented in Table 1. All the measuring equipment is interconnected by means of a General Purpose Interface Bus (GPIB) bus. Furthermore, a computer was connected to this bus, and executed the automated test programmed in Python (Version 3.9), which managed the entire test and stored and processed all the PCM measurements. Regarding the auxiliary boards, one of them was the same for TuMag and SCIP while the second one was different between both instruments. This second auxiliary board included the high-power dissipation loads mounted on an aluminium block provided with fans to avoid very high temperatures during the verification tests.

The PCM inrush current was characterised at all three input voltage levels (20.4 V, 25.6 V, and 29.2 V) to verify compatibility with the LCL power interface. The E-Unit was required to operate within defined constraints to ensure that its inrush current would not, under any circumstances, activate the LCL protection mechanism. Figure 9 shows the inrush current corresponding to the worst-case input condition (close to 7.5 A), confirming compliance with the specified limit (25 A).

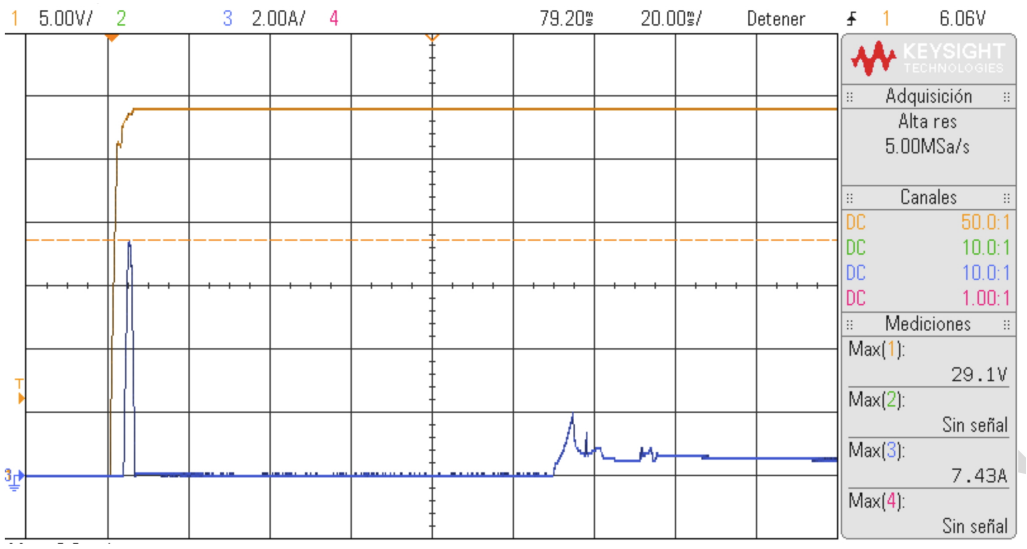


Figure 9. TuMag FM PCM inrush current profile. CH1 (orange): bus input voltage 5 V/div, CH3 (blue): bus input current 2.00 A/div.

As previously mentioned, a key objective of the project was to develop a PCM with an adaptable design that required only minimal modifications to meet the specific needs of both the TuMag and SCIP payloads. To this end, the PCM design and layout were conceived to accommodate the requirements of both instruments within a shared architectural framework. The SCIP PCM concept closely followed that of TuMag, based on a three-block architecture comprising DC/DC A, DC/DC B, and DC/DC C, with DC/DC A serving as the primary block and incorporating dedicated DM filters for each converter. However, SCIP did not require either the HVPS or the mechanisms associated with DC/DC A and DC/DC C in TuMag (see Figure 5), but it did integrate the PMU and SMM loads, both powered through the input voltage within the SCIP DC/DC C. Furthermore, the power demands for each output differed, as outlined in Table 1.

Collectively, these factors necessitated a flexible PCM design capable of accommodating the varying specifications. This design flexibility was a fundamental premise that contributed to optimising the development schedule and budget. Additionally, the initial functional verification campaign of one PCM BB facilitated the identification and correction of issues in the second BB of the other instrument, thereby streamlining the overall development process of the FMs for both instruments. Figure 10 illustrates the set-up employed for the verification of the SCIP PCM, incorporating a dedicated EGSE configured to simulate the load profile characteristic of the SCIP instrument.

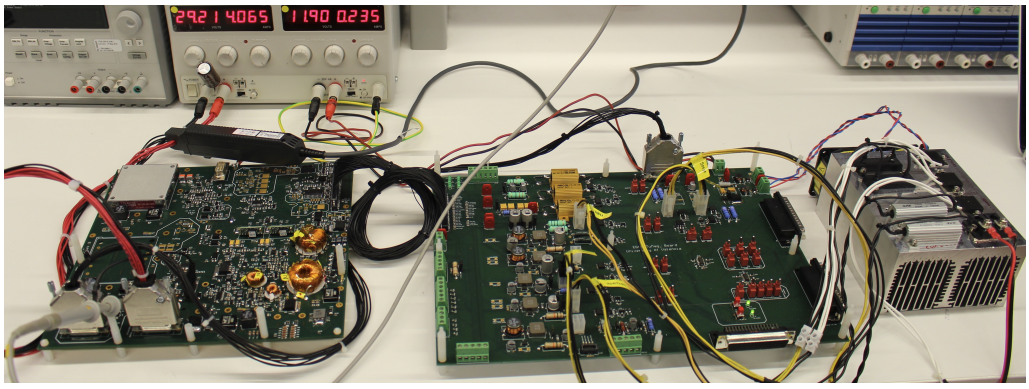


Figure 10. Set-up of the SCIP PCM and EGSE boards for the functional verification testing.

Finally, with regard to envelope and mass budget constraints, the limits remained consistent, with the SCIP PCM FM fully complying, as was the case with the TuMag PCM FM.

5. E-Unit Housing

The main electronics for TuMag and SCIP were located on the SUNRISE III electronics rack with connection lines to the O-Units. The E-Unit is a pressurised housing that contains a subset of electronic boards that comprises all the necessary devices to meet the requirements of the TuMag and SCIP instruments.

5.1. Design

Given that mainly commercial electronic components were used, it was considered essential to design a hermetically sealed E-Unit to ensure the reliable operation of the electronics. To mitigate the risks of condensation and humidity-induced malfunctions during the operational phase, characterised by low-pressure and fluctuating temperature conditions, the enclosure was filled with nitrogen. Moreover, the housing was pressurised to an overpressure of 1.1 bar at 20 °C, acknowledging that this pressure would vary in response to temperature changes during the ascent phase and flight.

The design philosophy adopted a "book-like" concept, whereby the enclosure is divided into two halves that open similarly to a book. This configuration facilitates the assembly of electronic components and their interconnections. Once assembled, the two halves are joined and sealed by a flange with an O-ring to prevent pressure loss. Internally, the enclosure is divided into two compartments: the lower half, closest to the rack, houses the HVPS and the PCM, while the upper half contains the DPU and the AMHD.

Constructed from aluminium alloy, the E-Unit features a rectangular geometry with rounded corners. In response to the requirement for minimal weight while maintaining optimal structural performance, the design incorporated a 4 mm wall thickness reinforced with stiffeners. Consequently, the total mass of the E-Unit housing was approximately 18 kg, remaining below the maximum limit specified by the project. Its external envelope, excluding the HV connector, measured 584 × 404 × 227 mm, thereby ensuring full compliance with both dimensional and mass constraints.

Furthermore, two valves from Schrader [41] for purging were located in the E-Unit base. They were located in opposite locations for better nitrogen circulation, providing an ambient without air, avoiding problems with the humidity as previously mentioned.

Two Schrader valves [41] for purging were installed at the base of the E-Unit, positioned opposite each other to optimise nitrogen circulation within the enclosure till the air was removed. This arrangement maintains an oxygen-free atmosphere, thereby preventing humidity-related issues as previously noted. Figure 11 illustrates a three-dimensional model of the E-Unit, with an arrow indicating the location of one such housing valve essential for pressure regulation.

To guarantee the required structural stiffness while minimising wall thickness and mass, the E-Unit incorporates both vertical and horizontal stiffeners. Additional design features affecting the final shape and thickness of the enclosure include accommodation for electrical connectors and attachment points for the legs, which interface the unit with the SUNRISE E-rack.

The number of fasteners used to attach the two halves was calculated following the methodology outlined in [42] to guarantee a uniform pressure distribution on the O-ring gasket. Accordingly, 50 screws were used to fasten the assembly.

All connectors required for data transmission and power supply—both low voltage and high voltage—are located predominantly on one side wall, except for two connectors

dedicated to the AMHD and the grounding interface. The connectors consist of D-Sub connectors from the XAVAC series manufactured by Positronics (Amphenol Corporation).

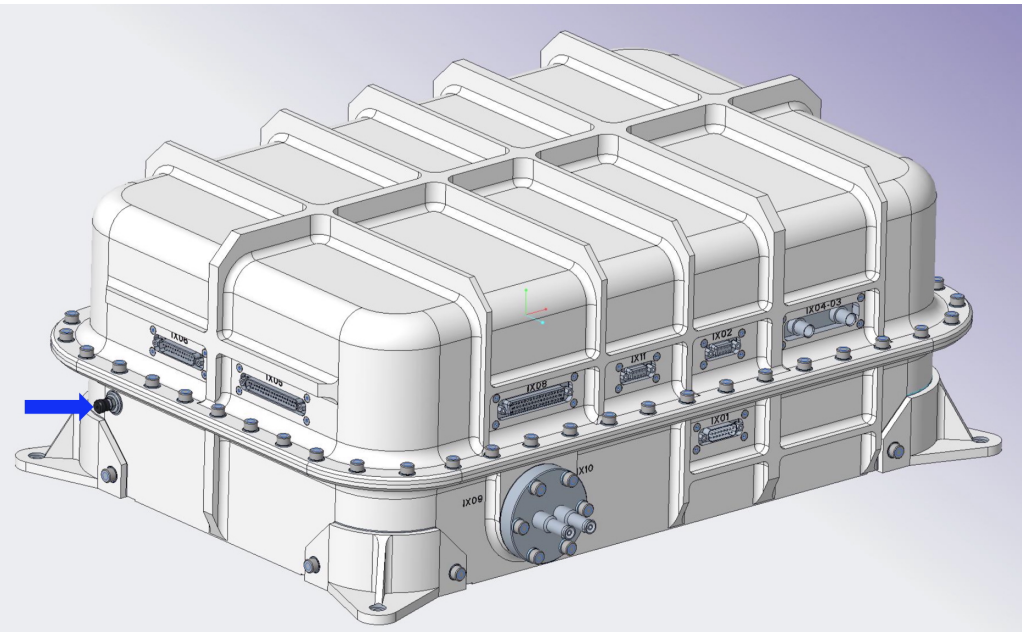


Figure 11. 3D model of the TuMag E-Unit highlighting a housing valve.

Each feedthrough D-Sub connector is sealed with an O-ring composed of material suitable for the low temperatures encountered during the ascent phase. Furthermore, the E-Unit is equipped with a DN40CF flange accommodating two high-voltage coaxial feedthrough connectors (SHV 20 kV). The HV connector is shown in Figures 11 and 12.

The mechanical interface with the E-rack platform is established through four feet situated at each corner of the housing, which are fastened to the E-rack via M6 screws. The legs provide a 1 mm elevation of the base, facilitating the placement of a thermal filler between the E-Unit and the E-rack. To optimise manufacturability and reduce the size of the main aluminium parts, the legs were designed as separate, modular elements.

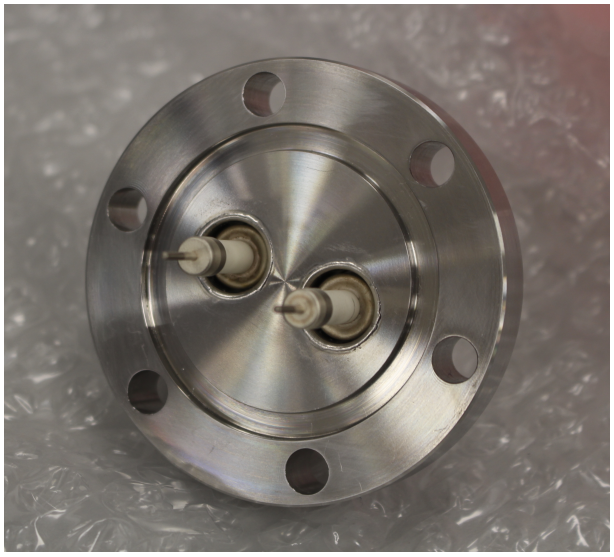


Figure 12. Connector for the HV required by the etalon.

5.2. Manufacturing and Test

5.2.1. Material Selection

During the initial design phase of the E-Unit's main structural components, both titanium and various aluminium alloys were evaluated. However, titanium was ultimately ruled out due to concerns regarding weight and cost. Aluminium alloys, by contrast, were selected not only for their favourable mass properties, but also for their compatibility in terms of the coefficient of thermal expansion (CTE) between the E-Unit and the gondola E-rack, which minimised undesirable stresses at the interface screws. Additionally, the use of aluminium facilitated optimisation of thermal conduction across the platform through the incorporation of thermal filler. As a result, this material selection was deemed optimal from both mechanical and thermal standpoints.

Initially, Al7075 alloy commonly employed in aerospace applications for its high yield strength was pre-selected. Subsequent analysis revealed a pronounced reduction in yield strength correlated inversely with material thickness, particularly significant beyond 120 mm. This drop in mechanical performance posed a critical limitation. Consequently, alternative alloys within the 7000 series were considered, culminating in the selection of Aluminium 7022 T651, which offers a more consistent strength profile relative to thickness and was deemed the most suitable choice.

Stainless Steel A4-80 was selected for critical screw products due to its higher yield strength, making it suitable for more demanding applications. In contrast, A2-70 was utilised for general-purpose fasteners, offering adequate performance for less critical elements.

For sealing applications subjected to stringent environmental conditions, a high-temperature vulcanised silicone elastomer (Vinyl Methyl Silicone, VMQ) was selected owing to its exceptional thermal and chemical stability. VMQ is a polysiloxane-based elastomer, featuring vinyl and methyl side groups, which confers outstanding resistance to elevated temperatures while retaining flexibility at cryogenic temperatures. Additionally, it exhibits robust stability against ultraviolet radiation, oxidative agents, and ozone, making it highly suitable for aerospace and vacuum technology applications requiring durable sealing solutions [43]. As discussed in [44], elastomer compositions are not standardised, and their exact formulations vary between manufacturers. This variability necessitates comprehensive characterisation to ensure material suitability for specific applications. Specialised VMQ variants such as fluorosilicone, Fluoro Vinyl Methyl Siloxane (FVMQ), offer enhanced chemical resistance and mechanical properties tailored to specific operational demands. The high friction coefficient of the VMQ restricts its application in dynamic sealing environments where alternative materials are available [43].

VMQ and FVMQ-based elastomers with tailored low-temperature formulations were selected to meet the thermal requirements associated with the mission's ascent phase. The operational lower temperature limit of the selected compounds was below the expected minimum during ascent. Standard silicone rubbers typically exhibit service temperature ranges from $-60\,^{\circ}\mathrm{C}$ to $230\,^{\circ}\mathrm{C}$, while specially engineered formulations may extend this range from $-100\,^{\circ}\mathrm{C}$ up to $250\,^{\circ}\mathrm{C}$ [45]. The specific formulation employed in this project was rated for continuous operation down to $-70\,^{\circ}\mathrm{C}$. The material specifications used for the unit sealing are summarized below:

- Main O-ring: dimensions 538 × 5 mm (Reference 70VMQS7063R-LT).
- High-voltage connector O-ring: dimensions 42 × 3 mm (Reference 70FVMQ).
- Feedthrough O-rings: manufactured from the same VMQ compound as the main O-ring.
- Lubricant: Apiezon N grease, characterised by low TML (<1%) and low CVCM (<0.1%), optimised for low-temperature and vacuum applications [46].

Achieving effective electrical and thermal conduction between the two principal subassemblies of the E-Unit was a key design requirement. Given the electrical insulating nature of VMQ O-rings, conductivity was ensured via mechanical fastening, employing 50 screws to secure the unit's components and guarantee reliable interface contact. Prior to integrating the fully populated PCBs, comprehensive leakage and fit tests were conducted. The housing was assembled with feedthrough connectors and an internal pressure sensor, which produces a voltage output proportional to internal pressure. Figure 13 depicts that assembly. The assembly was subjected to leak testing by pressurizing the housing to 1.1 bar at 20 °C above ambient pressure within a controlled climatic chamber. Temperature monitoring was implemented using five sensors—four affixed to external surfaces and one control sensor. The thermal cycling protocol ranged from −45 °C to 35 °C with a tolerance of ±3 °C, maintaining each temperature extreme for approximately 40 min. This cycle was repeated three times to simulate expected operational thermal fluctuations. Following the temperature cycles, the unit remained pressurised for several hours while pressure and temperature were continuously recorded. No leakage was detected throughout the testing, validating the sealing performance under the specified thermal and pressure conditions.

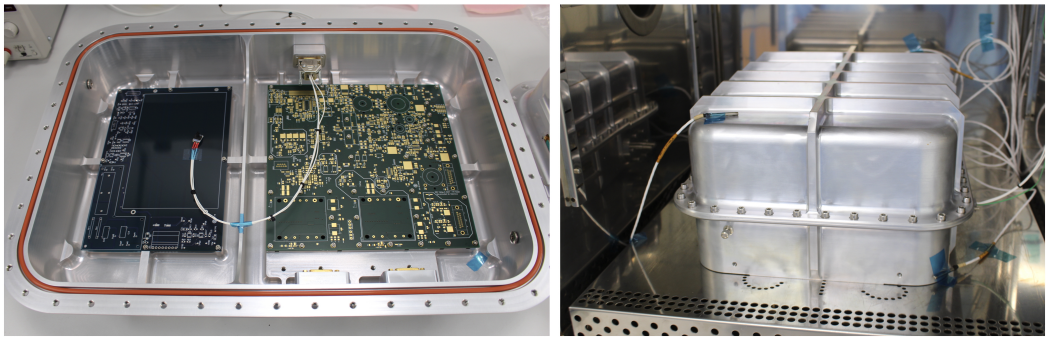


Figure 13. Fit-check of raw PCBs and O-ring validation (via thermal-vacuum chamber test) in the E-Unit prior to white painting.

5.2.2. Coating and Painting

In space applications, the application of a chemical conversion coating to machined aluminium components is essential for both protective and functional reasons. Among the various options available, SurTec 650V, a chromium(VI)-free passivation, was selected as the first surface treatment applied to the Aluminium 7022 T651 parts. This coating provides enhanced corrosion resistance, which is particularly critical for 7000-series aluminium alloys, especially in harsh pre-launch environments and in mitigating galvanic corrosion in multi-material assemblies. Additionally, SurTec 650V ensures adequate surface electrical conductivity, which is critical for Electromagnetic Compatibility (EMC), proper grounding, and electrostatic discharge mitigation within spacecraft structures. It provides a contact resistance lower than 5000 µΩ per square inch [47].

Beyond its protective and conductive properties, SurTec 650V also promotes strong adhesion for subsequent surface treatments, including primers for paint systems and structural adhesives. This contributes to long-term mechanical and thermal stability. Furthermore, its low outgassing behaviour makes it suitable for use in high-vacuum environments, where contamination of optical or thermal surfaces must be avoided. The product complies with European Cooperation for Space Standardization (ECSS) requirements, making it fully suitable for aerospace applications.

Following the chemical conversion process, the coated parts were white-painted to achieve the required thermo-optical properties, in particular surface emissivity. The paint selected was SG121-FD from MAP [48], a space-qualified white coating with established flight heritage. As required by the manufacturer, a primer was applied prior to paint-

ing (PSX [49]), resulting in a total thickness of approximately 100 to 140 µm. Specific areas—such as threaded and through holes, as well as all mating surfaces—were masked during the process to preserve high thermal and electrical conductivity where needed.

The outgassing characteristics of the selected paint were a critical consideration due to the proximity of sensitive optical elements, such as the telescope and the O-Units [50,51]. The relevant parameters are 0.28% for the RML; 0.08% for the CVCM; and 1.30% for the TML.

On one hand, the CVCM, which was considered the most critical parameter in the project, is below 0.1%. On the other hand, the TML value is just above the guideline limit. Despite being above the limit it was not considered a critical issue since the E-Unit was placed on the E-rack of the gondola, far from the ISLiD and the instrument O-Units. Nevertheless, an additional curing process (48 h at 70 °C), together with the thermal cycles of the E-Unit environmental test campaign, was performed to reduce the TML value closer or even below 1%.

Concerning the SCIP E-Unit housing design, it was largely derived from the TuMag configuration, sharing similar characteristics in terms of geometric envelope and allowable operational overpressure. The unit was specifically configured to accommodate the DPU, AMHD, and PCM boards, as SCIP did not require the integration of an HVPS board. Although the structural framework remained largely unchanged, the electrical interface requirements differed due to variations in connector types and harness layouts. Accordingly, minor design adaptations were implemented to meet the specific integration needs of the SCIP harness and connectors. This approach underscores the importance of modularity and design flexibility in the development of housings for complex electronic subsystems, contributing to improved development timelines and cost efficiency.

6. E-Unit Structural Analysis

6.1. Finite Elements Model

A Finite Element Model (FEM) was developed with MSC Patran [52] to analyse the E-Unit behaviour under the mechanical loads defined in this project. The goal of these analyses was to calculate the E-Unit low-frequency modes, to size its structural components based on the stresses obtained, and to analyse the PCBs displacement mainly due to the overpressure in flight, which is the most critical issue regarding the E-Unit structural feature on a stratospheric balloon project.

For the load conditions described in the next section, the required Margin of Safety (MoS) ratios were calculated. Additionally, design limit loads are amplified by a FoS to address uncertainties related to the statistical distribution of loads, structural analyses, manufacturing processes, material properties, and failure criteria [53].

The MoS is defined as

$$MoS = \frac{allowable\ load}{limit\ load \times FoS} - 1 \tag{4}$$

where the design allowable load considered was the yield limit of a material, and the applied limit load was the computed load under the defined load conditions.

6.2. Structural Analyses

The "book-like" enclosure, which positioned PCBs on opposing inner surfaces, required strict control of structural displacement to comply with deformation constraints. Maintaining minimal displacement under overpressure operating conditions was essential to prevent solder joint failures. Furthermore, the design played a key role in reducing thermo-elastic stresses arising from steep thermal gradients, particularly during the ascent

phase. Therefore, the results of the structural analysis were of utmost importance to avoid problems in the electronics of this unit.

The FEA was performed with MSC/NASTRAN structural solver and the post-processing by means of MSC Patran.

Although there was no requirement on the first eigenfrequency of the unit, a modal analysis was carried out in order to assess the global stiffness of the structure. As a result, two issues may be remarked: the first eigenfrequency obtained was 25 Hz at the HVPS board, and the accumulated mass in all axes up to 150 Hz is quite low, less than 15%. Moreover, the modes in this frequency range were due to the PCBs bending, while the E-Unit housing is quite rigid and its modes were above 150 Hz.

Table 4 shows the worst case of the quasi-static and thermo-elastic analyses. Regarding the quasi-static analysis the worst case was achieved in the E-Unit vertical axis, while for the thermo-elastic analysis the worst case is linked to its cold case in the ascent phase.

Table 4. Worst case stresses obtained from the quasi-static, thermo-elastic and overpressure analyses.

Analysis	Element	Level (MPa)	MoS
Quasi-static (vertical axis)	Housing Leg	63.2	3.7
	HVPS board	84.4	1.9
Thermo-elastic (cold case)	Housing lower part	183	0.6
	HVPS board	70.2	2.5
Overpressure (in-flight)	Housing upper part	182	0.4
	HVPS board	28.5	7.1

Moreover, one of the critical points of the project was the PCB distorsion and the Housing's flange separation due to the overpressure. The former may cause critical stresses on the soldering of the electronic components, and the latter would cause an undesirable leakage, and hence a loss of pressure and a partial exchange of nitrogen for humidity-laden air. The worst case results of the displacement analysis, considering a maximum overpressure of 1.27 bar, were as follows:

- Less than 0.1 mm of displacement over all the main flange.
- A displacement of 0.3 mm at the HVPS board.

Figure 14 displays the displacement analysis of the housing and of each PCB due to the pressure effect during flight, where the ambient pressure in operation is around 0.003 bar (300 Pa).

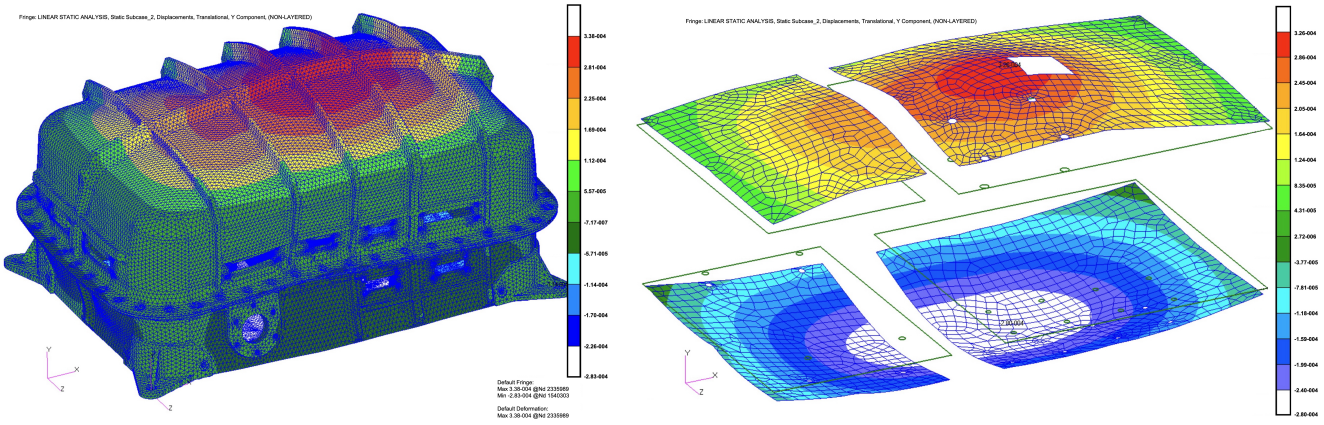


Figure 14. TuMag E-Unit housing (**left**) and electronic boards (**right**) displacement analysis due to the pressure effect during flight.

To avoid the air leakage, the O-ring had to be compressed at least 10% (0.5 mm). The design compression (at load free state) is 1 ± 0.15 mm (O-ring diameter 5 ± 0.1 mm and groove depth 4 ± 0.05 mm), being the most adverse manufacturing conditions a compression of 0.85 mm (allowing a maximum flange separation of 0.35 mm till the leakage limit).

As a conclusion, the structural analysis cases show a positive MoS in all the E-Unit elements.

7. In-Flight Telemetry

Figures 15–18 summarise key thermal and functional parameters of the PCM of the TuMag instrument recorded during the operational phase of the SUNRISE III flight, as well as the internal pressure of the E-Unit housing the PCM. These in-flight data, acquired by the PCM and associated sensors, provide detailed insight into the instrument's behaviour under operational conditions. Together, the figures confirm the correct functioning of the PCM, the pressurised enclosure, and the overall TuMag instrument, demonstrating stable performance throughout the mission.

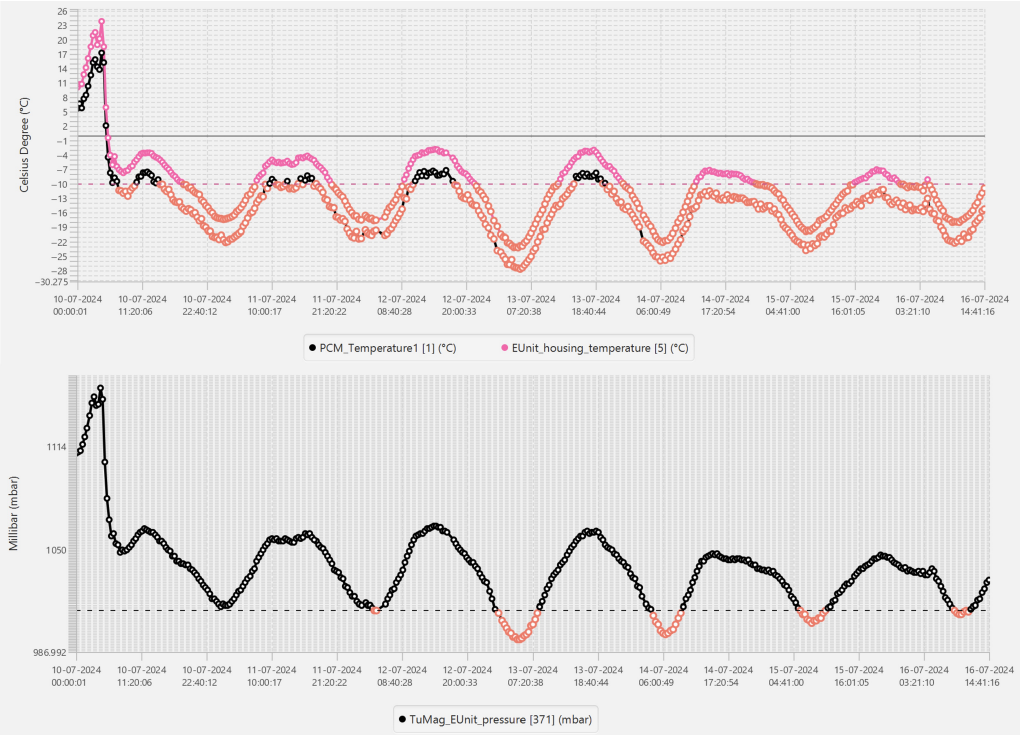


Figure 15. In-flight temperatures of TuMag E-Unit housing and PCM (**top**), and E-Unit pressure (**bottom**).

7.1. E-Unit Pressure Level

Figure 15 illustrates the temporal evolution of internal pressure within the E-Unit, alongside temperature readings from two sensors—one located on the PCM board and the other on the enclosure wall. The measured temperatures, ranging from approximately $-5\,^{\circ}$C to $-30\,^{\circ}$C, closely followed the pressure trend, consistent with the ideal gas law under constant volume.

This correlation indicates that the observed pressure variations were thermally induced, with no evidence of leakage or structural degradation. Final pressure values matched those at launch, confirming that the enclosure maintained its seal despite the harsh stratospheric environment. The dotted horizontal lines included in the plot serve purely as internal references and do not represent design limits.

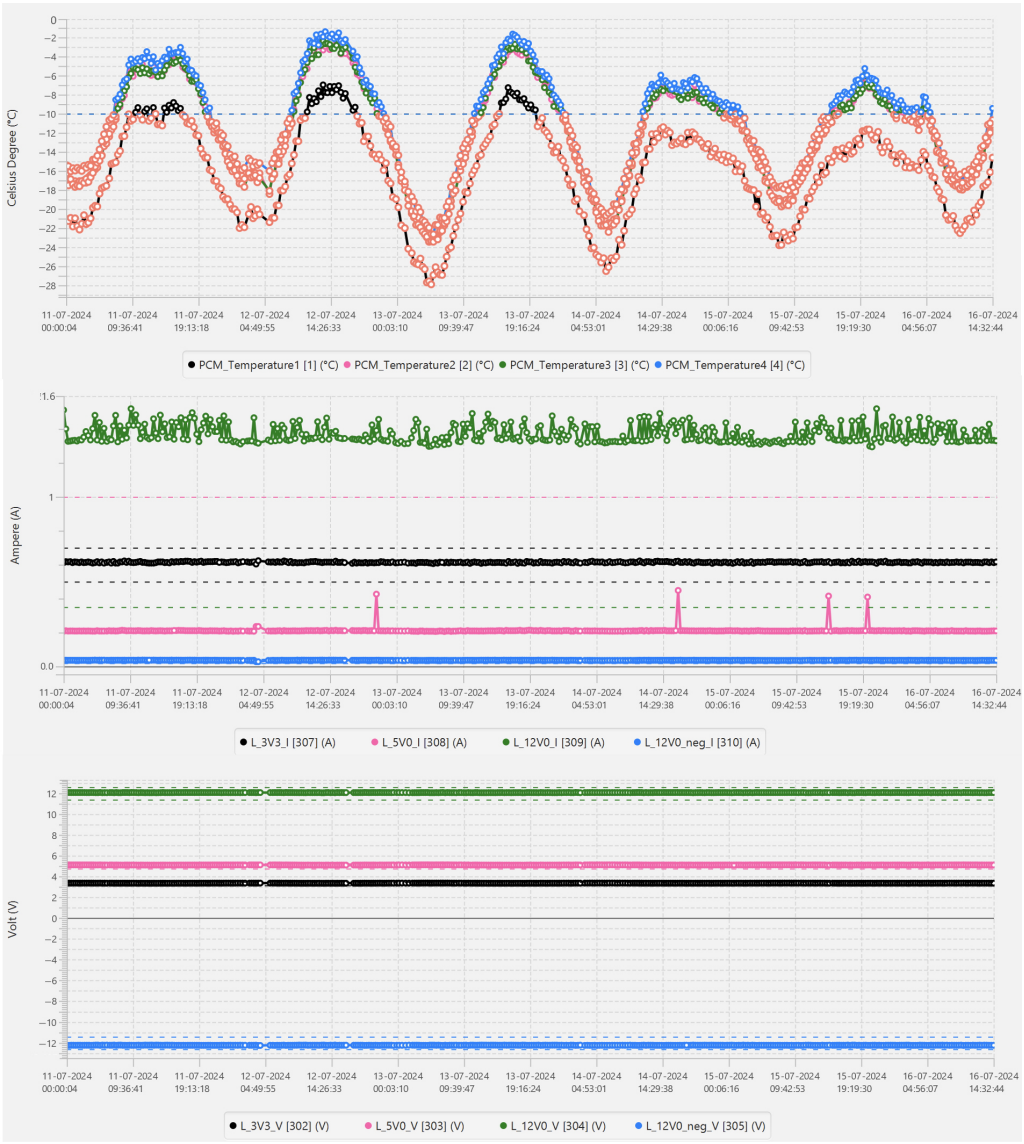


Figure 16. Temperatures vs. low voltages and currents of the TuMag PCM.

7.2. PCM Voltage, Current and Temperature Profiles

Thermal and electrical data from the PCM are shown in Figure 16, including temperature readings from four sensors mounted on the PCB, as well as current and voltage values for the +3.3 V, +5.0 V, +12 V, −12 V secondary power lines. These temperature measurements revealed variations of nearly 30 °C , indicative of the thermal cycling typical of stratospheric balloon flights.

Despite this environment, all low-voltage outputs remained stable and well within tolerance limits. This is particularly notable given the use of COTS components and the thermal stress encountered. No transient events or voltage deviations were observed, highlighting the robustness of the power regulation system.

Figure 17 provides current and voltage measurements for the +24 V supply lines, which power the Cameras and the HVPS. The cameras exhibited a steady current draw throughout the flight, in line with their continuous operation and need for supply stability. By contrast, the HVPS and associated mechanisms showed more variable current behaviour, as expected due to their intermittent operation (e.g., etalon tuning).

Nonetheless, the +24 V voltage levels remained consistently within specification, confirming the system's capacity to support subsystems with dynamic loads—such as the ±4 kV HVPS and imaging electronics, even under variable thermal and functional conditions.

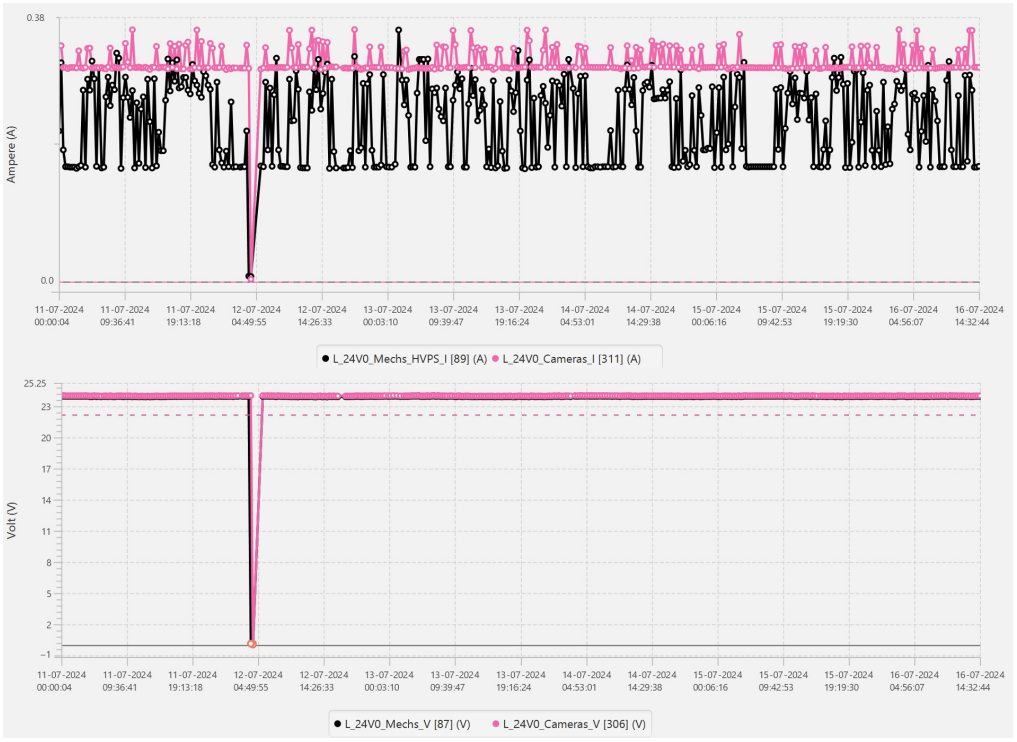


Figure 17. Secondary +24 V outputs of the TuMag PCM.

Lastly, Figure 18 details the primary power input delivered by the SUNRISE III platform, including the bus voltage supplied to the PCM and the total input current drawn by the TuMag instrument. Throughout the flight, the input voltage remained between 22.5 V and 28 V, and the current did not exceed 5.5 A.

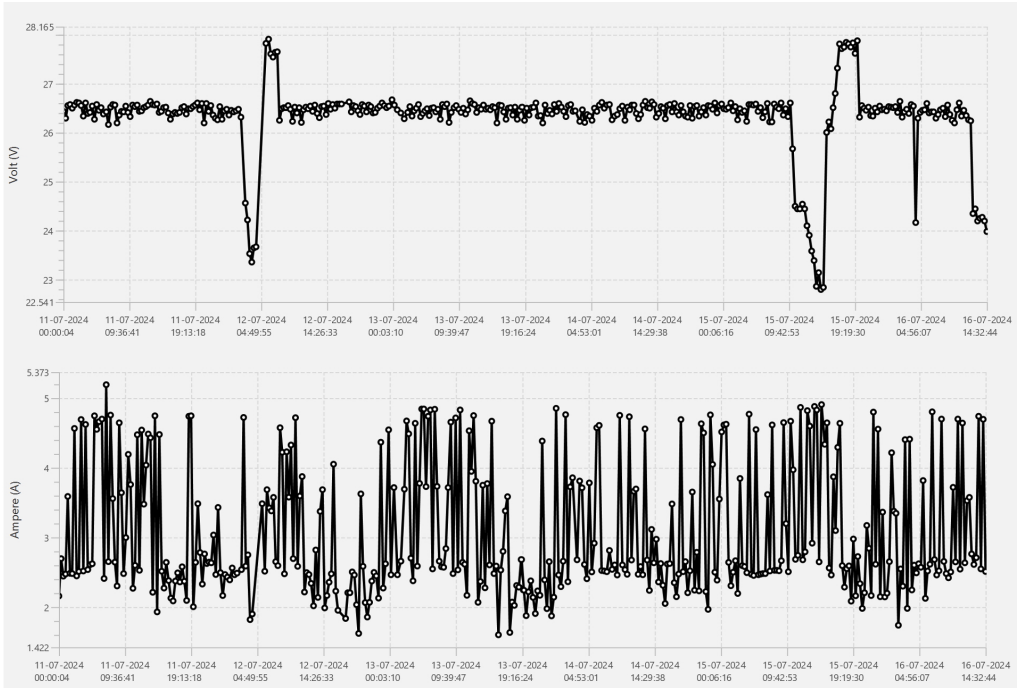


Figure 18. Input bus voltage and primary current of the TuMag PCM.

None of the PCM's protection mechanisms (UVLO, OVLO or overcurrent protection) were triggered at any time, indicating stable and reliable power provision from the platform.

These results confirm that the instrument operated well within its electrical design margins under actual flight conditions.

It is worth noting that scientific data acquisition was momentarily interrupted on two occasions due to anomalies in the platform's photovoltaic system. These events temporarily halted power delivery and triggered an automatic switch to battery mode. In both instances, solar input was restored, battery charging resumed, and normal instrument operation was re-established without lasting impact. The system's ability to manage these transitions autonomously highlights the resilience and reliability of the overall power architecture.

8. Conclusions

This work has presented the design, development, and in-flight validation of both the PCM and the pressurised E-Unit enclosure, integrated within the TuMag instrument onboard the SUNRISE III stratospheric balloon mission, launched in July 2024 from the ESRANGE Space Center in Kiruna, Sweden.

The PCM was designed to meet the stringent requirements of a complex scientific payload, delivering multiple regulated power lines to heterogeneous loads, including digital control units and a ± 4 kV HV supply for a Fabry–Pérot etalon. The system architecture combined a custom-designed master DC/DC converter with the use of COTS components for the remaining converters. The topology of the custom converter, along with the development of bespoke main magnetic components, is described in detail.

Particular attention was devoted to the design of these magnetic components, which incorporated novel techniques. Their successful in flight performance provides a solid basis for their use in power electronics systems of future high-altitude or spaceborne platforms.

The E-Unit enclosure was engineered to ensure operational integrity under the harsh environmental conditions characteristic of stratospheric balloon missions, particularly the extremely low temperatures encountered during ascent. Material selection and surface treatment were carried out with careful consideration of outgassing characteristics, critical for the protection of nearby optical elements. Structural features were analysed under mission-specific mechanical loads, with particular focus on enclosure leakage and potential deformation of electronic boards—both identified as critical design parameters.

Flexibility was also a key design driver. The system was conceived to allow adaptation, with minimal modifications, to the requirements of both TuMag and SCIP. This adaptability contributed to reduced development time and optimised overall project cost—two aspects of particular relevance in this context.

Telemetry data collected during flight confirmed the correct functioning of all subsystems. Internal pressure remained stable, and all power outputs maintained nominal voltage and current levels throughout the mission. These outcomes validate the performance, reliability, and environmental resilience of the developed systems under real stratospheric flight conditions.

These results not only demonstrate the reliability of the developed systems during the SUNRISE III mission, but also provide a valuable reference for future high-altitude balloon experiments and the design of robust power electronics for extreme environments like space.

Author Contributions: Conceptualization, J.L.G.-B., E.S.-K. and J.B.R.; Formal analysis, J.L.G.-B., E.S.-K., A.F. and D.G.; Funding acquisition, E.S.-K. and J.L.G.-B.; Investigation, J.L.G.-B.; Methodology, J.L.G.-B. and E.S.-K.; Project administration, J.L.G.-B.; Resources, J.L.G.-B., A.F. and D.G.; Supervision, E.S.-K.; Validation, J.L.G.-B., E.S.-K., A.F. and D.G.; Visualization, J.L.G.-B., J.B.R. and J.B.E.; Writing—original draft, J.L.G.-B.; Writing—review & editing, E.S.-K., D.G., J.B.R. and J.B.E. All authors have read and agreed to the published version of the manuscript.

Funding: This research was developed with the grant RTI2018-096886-B-C54 and the grant PID2021-125325OB-C54 funded by MCIN/AEI/10.13039/501100011033 and by 'ERDF A way of making Europe', and the grant PCI2022-135029-2 funded by MCIN/AEI/10.13039/501100011033 and by 'European Union NextGenerationEU/PRTR'.

Institutional Review Board Statement: Not applicable.

Informed Consent Statement: Not applicable.

Data Availability Statement: The data that support the findings of this study are available from the corresponding author, E. Sanchis Kilders (esteban.sanchis@uv.es), upon reasonable request.

Acknowledgments: The authors want to thank P. Rodríguez, M. Balaguer, D. Álvarez, A. López, and the S^{3}PC team and the SUNRISE team for their help in this work.

Conflicts of Interest: The authors declare no conflict of interest regarding the publication of this paper.

Abbreviations

The following abbreviations are used in this manuscript:

AMHD	Analog, Mechanisms & Heaters Drivers
APL	Johns Hopkins University Applied Physics Laboratory (USA)
BB	Breadboard
CM	Common Mode
CMAG	Coronal Magnetograph mission
COTS	Commercial-Off-The-Shelf
CSBF	Columbia Scientific Balloon Facility (USA)
CSIC	Consejo Superior de Investigaciones Científicas (Spain)
CTE	Coefficient of Thermal Expansion
CVCM	Collected Volatile Condensable Material
CWS	Correlating Wavefront Sensor
DM	Differential Mode
DPU	Data Processing Unit
E-Unit	Electronic Unit
ECSS	European Cooperation for Space Standardization
EGSE	Electrical Ground Support Equipment
EMC	Electromagnetic Compatibility
EMI	Electromagnetic Interference
ESA	European Space Agency
ESRANGE	ESRO Sounding Rocket Launching Range
ESRO	European Space Research Organisation
FEA	Finite Element Analysis
FEM	Finite Element Model
FM	Flight Model
FoS	Factor of Safety
FPGA	Field-Programmable Gate Array
FVMQ	Fluoro Vinyl Methyl siloxane (Fluorosilicone rubber)
GPIB	General Purpose Interface Bus
HV	High Voltage
HVPS	High Voltage Power Supply
IAA	Instituto de Astrofísica de Andalucía, CSIC (Spain)
IAC	Instituto de Astrofísica de Canarias (Spain)
IMaX	Imaging Magnetograph eXperiment
INTA	Instituto Nacional de Técnica Aeroespacial (Spain)
ISLiD	Image Stabilization and Light Distribution System
KIS	Leibniz-Institut für Sonnenphysik (Germany)
JAXA	Japan Aerospace Exploration Agency (Japan)

LCL	Latching Current Limiter
LDB	Long Duration Balloon
LDO	Low-Dropout
MoS	Margin of Safety
MPS	Max-Planck-Institut für Sonnensystemforschung (Germany)
NAOJ	National Astronomical Observatory of Japan (Japan)
NASA	National Aeronautics and Space Administration (USA)
OC	Overcurrent
O-Unit	Optical Unit
OVLO	Over-Voltage Lock-Out
PCB	Printed Circuit Board
PCM	Power Converter Module
PHI	Polarimetric and Helioseismic Imager
PMU	Polarization Modulation Unit
POL	Point-Of-Load
PTFE	Polytetrafluoroethylene
PWM	Pulse Width Modulator
RML	Recovered Mass Loss
S^3PC	Spanish Space Solar Physics Consortium
SCIP	SUNRISE Chromospheric Infrared spectro-Polarimeter
SMM	Scan Mirror Mechanism
SSC	Swedish Space Corporation (Sweden)
SUSI	SUNRISE Ultraviolet Spectropolarimeter and Imager
TML	Total Mass Loss
TuMag	Tunable Magnetograph
UPM	Universidad Politécnica de Madrid (Spain)
UV	University of Valencia (Spain)
UVLO	Under-Voltage Lock-Out
VMQ	Vinyl Methyl Silicone

References

1. Pang, C.; He, Z.; Song, K.; Cao, S. Analysis of Wind Field Response Characteristics of Tethered Balloon Systems. *Aerospace* **2024**, *11*, 360. [CrossRef]
2. Witte, L.; Arnold, G.; Bertram, J.; Grott, M.; Krämer, C.; Lorek, A.; Wippermann, T. A Concept for a Mars Boundary Layer Sounding Balloon: Science Case, Technical Concept and Deployment Risk Analysis. *Aerospace* **2022**, *9*, 136. [CrossRef]
3. Ligterink, N.F.W.; Kipfer, K.A.; Gruchola, S.; Boeren, N.J.; Keresztes Schmidt, P.; de Koning, C.P.; Tulej, M.; Wurz, P.; Riedo, A. The ORIGIN Space Instrument for Detecting Biosignatures and Habitability Indicators on a Venus Life Finder Mission. *Aerospace* **2022**, *9*, 312. [CrossRef]
4. Agrawal, R.; Buchanan, W.P.; Arora, A.; Girija, A.P.; De Jong, M.; Seager, S.; Petkowski, J.J.; Saikia, S.J.; Carr, C.E.; Grinspoon, D.H.; et al. Mission Architecture to Characterize Habitability of Venus Cloud Layers via an Aerial Platform. *Aerospace* **2022**, *9*, 359. [CrossRef]
5. Buchanan, W.P.; de Jong, M.; Agrawal, R.; Petkowski, J.J.; Arora, A.; Saikia, S.J.; Seager, S.; Longuski, J.; on behalf of the Venus Life Finder Mission Team. Aerial Platform Design Options for a Life-Finding Mission at Venus. *Aerospace* **2022**, *9*, 363. [CrossRef]
6. Hubert, G.; Bezerra, F.; Nicot, J.M.; Artola, L.; Cheminet, A.; Valdivia, J.N.; Mouret, J.M.; Meyer, J.R.; Cocquerez, P. Atmospheric Radiation Environment Effects on Electronic Balloon Board Observed During Polar Vortex and Equatorial Operational Campaigns. *IEEE Trans. Nucl. Sci.* **2014**, *61*, 1703–1709. [CrossRef]
7. Wrobel, F.; Vaille, J.R.; Pantel, D.; Dilillo, L.; Rech, P.; Galliere, J.M.; Touboul, A.; Chadoutaud, P.; Cocquerez, P.; Lacourty, M.; et al. Experimental Characterization of an Atmospheric Environment With a Stratospheric Balloon. *IEEE Trans. Nucl. Sci.* **2011**, *58*, 945–951. [CrossRef]
8. Sirks, E.L.; Massey, R.; Gill, A.S.; Anderson, J.; Benton, S.J.; Brown, A.M.; Clark, P.; English, J.; Everett, S.W.; Fraisse, A.A.; et al. Data Downloaded via Parachute from a NASA Super-Pressure Balloon. *Aerospace* **2023**, *10*, 960. [CrossRef]
9. CNES. CNES Balloon Programme. 2005. Available online: https://cnes.fr/en/projects/ballons (accessed on 27 July 2025).
10. ESA. BEXUS Programme. 2005. Available online: https://rexusbexus.net (accessed on 27 July 2025).
11. CSBF. NASA Columbia Scientific Balloon Facility. 2024. Available online: https://www.csbf.nasa.gov (accessed on 27 July 2025).

12. Yajima, N.; Izutsu, N.; Imamura, T.; Abe, T. *Scientific Ballooning. Technology and Applications of Exploration Balloons Floating in the Stratosphere and the Atmospheres of Other Planets*, 1st ed.; Springer: New York, NY, USA, 2009. [CrossRef]
13. Gemignani, M.; Marcuccio, S. Dynamic Characterization of a High-Altitude Balloon during a Flight Campaign for the Detection of ISM Radio Background in the Stratosphere. *Aerospace* **2021**, *8*, 21. [CrossRef]
14. Naumann, P.; Sands, T. Micro-Satellite Systems Design, Integration, and Flight. *Micromachines* **2024**, *15*, 455. [CrossRef]
15. del Toro Iniesta, J.C.; Orozco Suárez, D.; Álvarez-Herrero, A.; Sanchis Kilders, E.; Pérez-Grande, I.; Ruiz Cobo, B.; Bellot Rubio, L.R.; Balaguer Jiménez, M.; López Jiménez, A.C.; Álvarez García, D.; et al. TuMag: The tunable magnetograph for the SUNRISE III mission. *Sol. Phys.* **2025**. [CrossRef]
16. Staliulionis, Z.; Mohanty, S.; Hattel, J.H.; Miliauskas, G. Numerical Modelling of Humidity Behaviour in the Electronics Housing. In Proceedings of the 2022 26th International Conference Electronics, Palanga, Lithuania, 13–15 June 2022; pp. 1–6. [CrossRef]
17. Deaconescu, A.; Deaconescu, T. Behavioral Study of Elastomeric O-Rings Built into Coaxial Sealing Systems. *Polymers* **2025**, *17*, 1275. [CrossRef] [PubMed]
18. Barthol, P.; Gandorfer, A.; Solanki, S.K.; Schüssler, M.; Chares, B.; Curdt, W.; Deutsch, W.; Feller, A.; Germerott, D.; Grauf, B.; et al. The Sunrise Mission. *Sol. Phys.* **2011**, *268*, 1–34. [CrossRef]
19. Solanki, S.K.; Riethmüller, T.L.; Barthol, P.; Danilovic, S.; Deutsch, W.; Doerr, H.-P.; Feller, A.; Gandorfer, A.; Germerott, D.; Gizon, L.; et al. The Second Flight of the Sunrise Balloon-borne Solar Observatory: Overview of Instrument Updates, the Flight, the Data, and First Results. *Astrophys. J. Suppl. Ser.* **2017**, *229*, 2. [CrossRef]
20. Korpi-Lagg, A.; Gandorfer, A.; Solanki, S.K.; del Toro Iniesta, J.C.; Katsukawa, Y.; Bernasconi, P.; Berkefeld, T.; Feller, A.; Riethmüller, T.L.; Álvarez-Herrero, A.; et al. SUNRISE III: Overview of Observatory and Instruments. *Sol. Phys.* **2025**, *300*, 75. [CrossRef]
21. Bernasconi, P.; Carpenter, M.; Eaton, H.; Schulze, E.; Carkhuff, B.; Palo, G.; Young, D.; Raouafi, N.; Vourlidas, A.; Coker, R.; et al. The Gondola for the SUNRISE III Balloon-Borne Solar Observatory. *Sol. Phys.* **2025**, *300*, 112. [CrossRef]
22. Solanki, S.K.; del Toro Iniesta, J.C.; Woch, J.; Gandorfer, A.; Hirzberger, J.; Alvarez-Herrero, A.; Appourchaux, T.; Martínez Pillet, V.; Pérez-Grande, I.; Sanchis Kilders, E.; et al. The Polarimetric and Helioseismic Imager on Solar Orbiter. *Astron. Astrophys.* **2020**, *642*, A11. [CrossRef]
23. García Marirrodriga, C.; Pacros, A.; Strandmoe, S.; Arcioni, M.; Arts, A.; Ashcroft, C.; Ayache, L.; Bonnefous, Y.; Brahimi, N.; Cipriani, F.; et al. Solar Orbiter: Mission and Spacecraft Design. *Astron. Astrophys.* **2021**, *646*, A121. [CrossRef]
24. Jones, W.V. The US Long Duration Balloon Facility at McMurdo Station. In Proceedings of the International Astronomical Union 2012, Beijing, China, 20–31 August 2013; International Astronomical Union: Paris, France, 2013; Volume 8, pp. S288, 169–177. [CrossRef]
25. Pacheco, L.E. Stratospheric Catalogue. 2022. Available online: https://stratocat.com.ar (accessed on 27 July 2025).
26. Corporation, S.S. ESRANGE Space Center. 2021. Available online: https://sscspace.com/esrange/ (accessed on 27 July 2025).
27. S^3PC. Spanish Space Solar Physics Consortium. 2022. Available online: https://s3pc.es (accessed on 27 July 2025).
28. Feller, A.; Gandorfer, A.; Grauf, B.; Hölken, J.; Iglesias, F.A.; Korpi-Lagg, A.; Riethmüller, T.L.; Staub, J.; Fernandez-Rico, G.; Castellanos Durán, J.S.; et al. The Sunrise Ultraviolet Spectropolarimeter and Imager: Instrument Description. *Sol. Phys.* **2025**, *300*, 65. [CrossRef]
29. Katsukawa, Y.; del Toro Iniesta, J.C.; Solanki, S.K.; Kubo, M.; Hara, H.; Shimizu, T.; Oba, T.; Kawabata, Y.; Tsuzuki, T.; Uraguchi, F.; et al. The Sunrise Chromospheric Infrared Spectro-Polarimeter SCIP: An Instrument for SUNRISE III. *Sol. Phys.* 2025, *submitted*.
30. Orozco Suárez, D.; del Toro Iniesta, J.C.; Bailén Martínez, F.J.; Balaguer Jiménez, M.; Álvarez García, D.; Serrano, D.; Peñin, L.F.; Vázquez-Ramos, A.; Bellot Rubio, L.R.; Atienzar, J.; et al. CMAG: A Mission to Study and Monitor the Inner Corona Magnetic Field. *Aerospace* **2023**, *10*, 987. [CrossRef]
31. Cao, S.; Yang, Y.; Zhang, H.; Zhao, R.; Zhu, R.; Zhang, D.; Song, L. Ascending Performance of Scientific Balloons with Buoyant Gas–Air Mixture Inflation for Designated Ceiling Height. *Aerospace* **2024**, *11*. [CrossRef]
32. Pérez-Grande, I.; Sanz-Andrés, A.; Bezdenejnykh, N.; Barthol, P. Transient Thermal Analysis during the Ascent Phase of a Balloon-borne Payload. Comparison with SUNRISE Test Flight Measurements. *Appl. Therm. Eng.* **2009**, *29*, 1507–1513. [CrossRef]
33. Tang, J.; Pu, S.; Yu, P.; Xie, W.; Li, Y.; Hu, B. Research on Trajectory Prediction of a High-Altitude Zero-Pressure Balloon System to Assist Rapid Recovery. *Aerospace* **2022**, *9*, 622. [CrossRef]
34. Fernández-Soler, A.; González-Bárcena, D.; Grande, I.; Sanz-Andres, A. Thermal Analysis of SUNRISE III Ascent Phase. In Proceedings of the 50th Conference on Environmental Systems. International Conference on Environmental Systems, Lisbon, Portugal, 12–14 July 2021 Available online: https://hdl.handle.net/2346/87142 (accessed on 27 July 2025).
35. Liu, Q.; He, L.; Yang, Y.; Zhao, K.; Li, T.; Zhu, R.; Wang, Y. The Influence of Ice Accretion on the Thermodynamic Performance of a Scientific Balloon: A Simulation Study. *Aerospace* **2024**, *11*, 899. [CrossRef]
36. MeteoSwiss. Federal Office of Meteorology and Climatology MeteoSwiss. 2025. Available online: https://www.meteoswiss.admin.ch/climate/the-climate-of-switzerland/annual-cycle-of-temperature-precipitation-and-sunshine/annual-cycle-of-the-tropopause-height.html (accessed on 27 July 2025).

37. Gilabert-Palmer, D.; Sanchis-Kilders, E.; Esteve, V.; Ferreres, A.; Ejea, J.B.; Maset, E.; Jordán, J.; Dede, E. Measuring Coupling Coefficient of Windings With Dissimilar Turns' Number or Tight Coupling Using Resonance. *IEEE Trans. Power Electron.* **2018**, *33*, 9790–9802. [CrossRef]
38. Gilabert, D.; Sanchis-Kilders, E.; Martínez, P.J.; Maset, E.; Ferreres, A.; Esteve, V. Zero Ripple Current With Coupled Inductors in Continuous Conduction Mode Under PWM Signals. *IEEE J. Emerg. Sel. Top. Power Electron.* **2020**, *8*, 4260–4269. [CrossRef]
39. Gilabert, D.; Sanchis-Kilders, E.; Martínez, P.J.; Maset, E.; Ferreres, A.; Esteve, V. Design of Zero-Ripple-Current Coupled Inductors With PWM Signals in Continuous Conduction Mode. *IEEE Trans. Ind. Electron.* **2021**, *68*, 304–311. [CrossRef]
40. *ECSS-E-HB-10-02A*; Requirements, E.; Division, S. Verification Guidelines. European Cooperation for Space Standardization, Noordwijk: The Netherlands, 2010. Available online: https://ecss.nl/hbstms/ecss-e-10-02a-verification-guidelines/ (accessed on 27 July 2025).
41. Pacific, S. Schrader Pacific Datasheet. Datasheet, Schrader s.a.s, Pontarlier Cedex—France. 2021. Available online: https://schrader-pacific.fr/en (accessed on 27 July 2025).
42. Flitney, R. *Seals and Sealing Handbook*; Elsevier, Ltd.: Amsterdam, The Netherlands, 2014. [CrossRef]
43. ERIKS. ERIKS. 2020. Available online: https://eriks.com/en/ (accessed on 27 July 2025).
44. Jousten, K. *Handbook of Vacuum Technology*; Wiley-VCH Verlag GmbH & Co. KGaA: Weinheim, Germany, 2016; ISBN: 978-3-527-41338-6. Available online: https://onlinelibrary.wiley.com/doi/epdf/10.1002/9783527688265.fmatter (accessed on 27 July 2025).
45. EPIDOR. EPIDOR Seals and Rubber Technology. Datasheet, EPI industries, Barcelona, Spain, 2025. Available online: https://www.epi-industries.com/en/companies/#epidor-seals-and-rubber-technology (accessed on 27 July 2025).
46. Apiezon. APIEZON Ultra High and High Vacuum Greases. Datasheet, APIEZON, 2018. Available online: https://apiezon.com/products/vacuum-greases/apiezon-n-grease/ (accessed on 27 July 2025).
47. SurTec. Surtec 650V datasheet. Datasheet, SurTec International GmbH, Bensheim, Germany, 2019. Available online: https://www.surtec.com/en/products-services/surtec-650-v/ (accessed on 27 July 2025).
48. MAP. MAP SG121-FD White Silicone Coating Low Outgassing. Datasheet, MAP Space Coating, Mazères, France, 2019. Available online: https://www.map-coatings.com/web/content/116829?unique=37255549cfa3b57f0f19c3957064fec122c0ff36 (accessed on 27 July 2025).
49. MAP. MAP PSX: Adhesion Primer for space use. Technical data sheet. Datasheet, MAP Space Coating, Mazères, France, 2016. Available online: https://www.map-coatings.com/en_US/ (accessed on 27 July 2025).
50. *ECSS-Q-ST-70-02C*; Requirements, E.; Division, S. Space Product Assurance: Thermal Vacuum Outgassing Test for the Screening of Space Materials. European Cooperation for Space Standardization: Noordwijk, The Netherlands, 2008. Available online: https://ecss.nl/standard/ecss-q-st-70-02c-thermal-vacuum-outgassing-test-for-the-screening-of-space-materials/ (accessed on 27 July 2025).
51. Guo, Q.; Liu, Y.; Mao, S.; Zhang, H.; Chen, L.; Liu, S.; Chen, B. Outgassing Test of Contamination Sensitive Unit for Space Optical Instruments. In Proceedings of the AOPC 2020: Telescopes, Space Optics, and Instrumentation, Beijing, China, 30 November–2 December 2020; Xue, S., Zhang, Z., Eds.; International Society for Optics and Photonics, 2020; Volume 11570, pp. 67–71. [CrossRef]
52. AB, H. Hexagon AB (Patran and MSC Nastran). 2025. Available online: https://hexagon.com (accessed on 27 July 2025).
53. *ECSS-E-ST-32-10C Rev.2, Corr.1*; Requirements, E.; Division, S. Space Engineering: Structural Factors of Safety for Spaceflight Hardware European Cooperation for Space Standardization: Noordwijk, The Netherlands, 2019. Available online: https://ecss.nl/standard/ecss-e-st-32-10c-rev-2-corr-1-structural-factors-of-safety-for-spaceflight-hardware-1-august-2019/ (accessed on 27 July 2025).

Disclaimer/Publisher's Note: The statements, opinions and data contained in all publications are solely those of the individual author(s) and contributor(s) and not of MDPI and/or the editor(s). MDPI and/or the editor(s) disclaim responsibility for any injury to people or property resulting from any ideas, methods, instructions or products referred to in the content.